

Morphological and architectural evolution of submarine channels: An example from the world's largest submarine fan in the Bay of Bengal

Dongwei Li^{a,b}, Chenglin Gong^{a,b,*}, Guozhang Fan^c, Ronald J. Steel^d, Daoyao Ge^b, Dali Shao^c, Liangbo Ding^c

^a State Key Laboratory of Petroleum Resources and Prospecting, China University of Petroleum (Beijing), Beijing, 102249, China

^b College of Geosciences, China University of Petroleum (Beijing), Beijing, 102249, China

^c PetroChina Hangzhou Research Institute of Geology, Hangzhou, Zhejiang 310023, China

^d Department of Geological Sciences, Jackson School of Geosciences, University of Texas, Austin, TX, 78712, USA

ARTICLE INFO

Keywords:

Bengal fan

Submarine channels

Types of CCSs

Channel evolution

Waxing-then-waning energy cyclicity

ABSTRACT

The characteristics and evolution of different types of channel-complex sets (CCSs) have long attracted attention from both academia and the oil industry. 3D seismic data from the world's largest submarine fan in the Bay of Bengal allow the exploration of morphology, architecture, and evolution of a Pleistocene submarine channel system from inception to abandonment. Four types of architectural elements are recognized, including feeder and distributary channel-complex set (CCS), levees, bend cutoffs, and incised and unincised crevasse splays. Three types of CCSs are recognized: (1) erosional non-leveed CCSs with the lowest values of channel width (W), thickness (T), and cross-sectional area (C_a) (mean values of $W = 153$ m, $T = 20$ m, and $C_a = 2613$ m²); (2) graded CCSs with the highest values of W , T and C_a (mean values of $W = 745$ m, $T = 89$ m, and $C_a = 49183$ m²); (3) aggradational leveed CCSs with intermediate values of W , T and C_a (mean values of $W = 476$ m, $T = 56$ m, and $C_a = 21968$ m²). Graded CCSs and aggradational leveed CCSs have overbank levees, crevasse splays and bend cutoffs, whereas erosional non-leveed CCSs lack these features. Such architectural difference in overbank deposits suggests a channel evolution pattern of initial incision (erosional non-leveed CCSs) and then aggradation (graded and aggradational leveed CCSs), resulting in a pattern of incision-to-aggradation channel evolution. An increase-then-decrease in channel morphometrics (represented by W , T , and C_a) from erosional non-leveed CCSs with the lowest mean values of W , T , and C_a , to graded CCSs with the highest mean values of W , T , and C_a , and finally to aggradational leveed CCSs with the intermediate mean values of W , T , and C_a suggest that the incision-to-aggradation channel evolution is related to waxing-then-waning energy cyclicity. Submarine channel turbidity flows during the waxing energy phase became progressively more energetic and increasingly more erosional, producing erosional non-leveed CCSs. Instead, submarine channel turbidity flows during the waning energy phase were more diluted and increasingly more depositional, thereby producing aggradational leveed CCSs. The phase of peak environmental energy was most likely accompanied by most energetic turbidity currents, resulting in graded CCSs. Results and observations from the current study contribute to a better understanding of architectural complexity and evolution of submarine channels.

1. Introduction

Submarine canyons and channels have been the focus of extensive research since their discovery in the 19th century (e.g., Buchanan, 1887; Daly, 1936; Shepard and Emery, 1941; Peakall and Sumner, 2015; Fildani, 2017). They can be up to several to tens of kilometers wide, and can extend for tens to thousands of kilometers on the modern seafloor (Peakall and Sumner, 2015; Heijnen et al., 2020). They play the role of

the major conduits for the delivery of large amounts of sediment, nutrients, pollutants, and organic carbon down to deep-water areas (Galy et al., 2007; Hughes Clarke, 2016; Symons et al., 2017; Hage et al., 2020). Sediment gravity flows in submarine channels pose a threat to undersea pipelines and telecommunication cables that carry 95% of transoceanic data traffic (Carter et al., 2009). Deposits in submarine channels preserve critical signals of paleoceanographic and paleoclimatic information from their source regions, and therefore act as an

* Corresponding author: State Key Laboratory of Petroleum Resources and Prospecting, China University of Petroleum (Beijing), Beijing, 102249, China.

E-mail address: chenglingong@cup.edu.cn (C. Gong).

<https://doi.org/10.1016/j.marpetgeo.2023.106368>

Received 1 April 2023; Received in revised form 6 June 2023; Accepted 7 June 2023

Available online 14 June 2023

0264-8172/© 2023 Elsevier Ltd. All rights reserved.

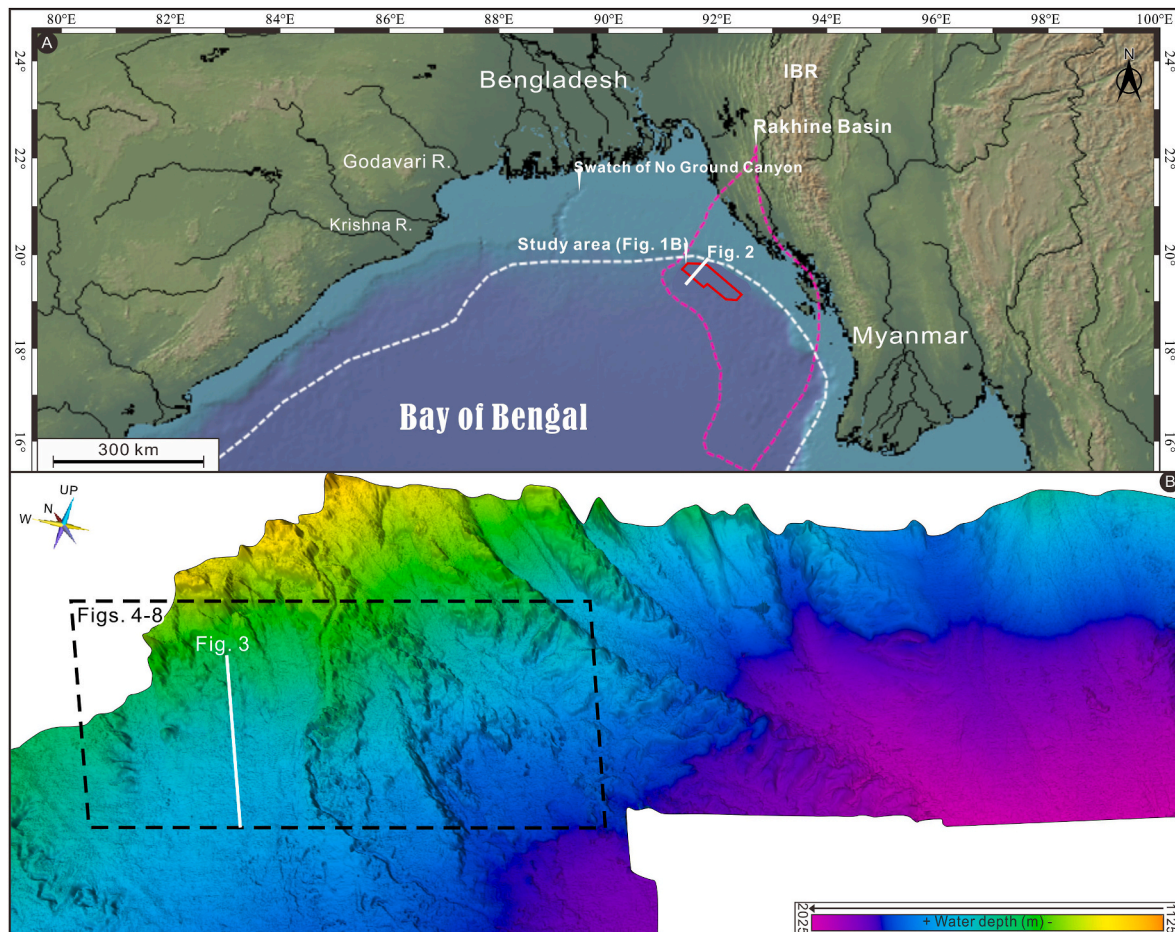


Fig. 1. (A) Regional map of the Ganges-Brahmaputra sediment-dispersal system showing regional map-view location of 2D seismic profile shown in Fig. 2 and the geographic context of the study area in the Rakhine Basin (IBR = Indo-Burman Range, Godavari R. = Godavari River, and Krishna R. = Krishna River). (B) 3D perspective of the modern seafloor showing plan-view locations of seismic line shown in Fig. 3, and RGB spectral decomposition-attribute and RMS amplitude maps shown in Fig. 4–8.

archive for the Earth's history (Prins and Postma, 2000; Clift and Gae-dicke, 2002). Submarine channels are the primary elements building the largest sedimentary accumulations of the planet (i.e., submarine fans) (Peakall and Sumner, 2015; Gong et al., 2022), and can form major subsurface oil and gas reservoirs in locations worldwide with considerable economic and strategic significance (e.g., Kolla et al., 2001; Abreu et al., 2003; Posamentier and Kolla, 2003; Mayall et al., 2006; Janocko et al., 2013).

The past two decades witnessed significant advances in the sedimentological understanding of submarine channels and their associated architectural elements, including channel fills (e.g., Deptuck et al., 2003, 2007; Mayall et al., 2006; Clark and Cartwright, 2011; McHargue et al., 2011; Janocko et al., 2013; Oluboyo et al., 2014; Bouchakour et al., 2022), lateral accretion packages (Abreu et al., 2003; Mayall et al., 2006, 2010; Kolla, 2007; Wynn et al., 2007; Janocko et al., 2013; Bouchakour et al., 2022, 2023), non-turbiditic mass-transport complexes (Deptuck et al., 2003; Tek et al., 2021), terraces (Babonneau et al., 2004; Hansen et al., 2017), and levees (Posamentier and Kolla, 2003; Kane et al., 2007; Jobe et al., 2015; Mitchell et al., 2021a, 2021b). In recent years, an increasing effort has been made to understand flow dynamics and structures of turbidity currents operating within submarine channels, through direct field measurements (e.g., Azpiroz-Zabala et al.,

2017; Paull et al., 2018) and detailed time-lapse seabed surveys (e.g., Vendettuoli et al., 2019; Heijnen et al., 2020).

During the last few decades, architecture, morphometrics, and evolution of submarine channels have been an important research focus (e.g., Schwenk et al., 2005; Hubbard et al., 2011; Fildani et al., 2013; Sylvester and Covault, 2016; Guiastrennec-Faugas et al., 2021). Despite their significance and many years of study, a clear understanding of submarine channel evolution and stratigraphic architecture from inception to abandonment remains elusive (Sylvester and Covault, 2016; Guiastrennec-Faugas et al., 2021). Using commercially acquired 3D seismic datasets from the world's largest submarine fan in the Bay of Bengal (Fig. 1), we attempt to: (1) explore how channel architectures and morphometrics evolve from their inception to abandonment; (2) investigate three types of channel-complex sets (CCSs) and their characteristics; and (3) investigate the evolution of CCSs and their controls. Addressing these research objectives will enable a better understanding of architectural complexity and evolution of submarine channels.

2. Geological background of the study area

The study area is located in the Rakhine Basin in the northeastern fringe of the upper Bengal Fan (Fig. 1A). The Bengal Fan is the largest

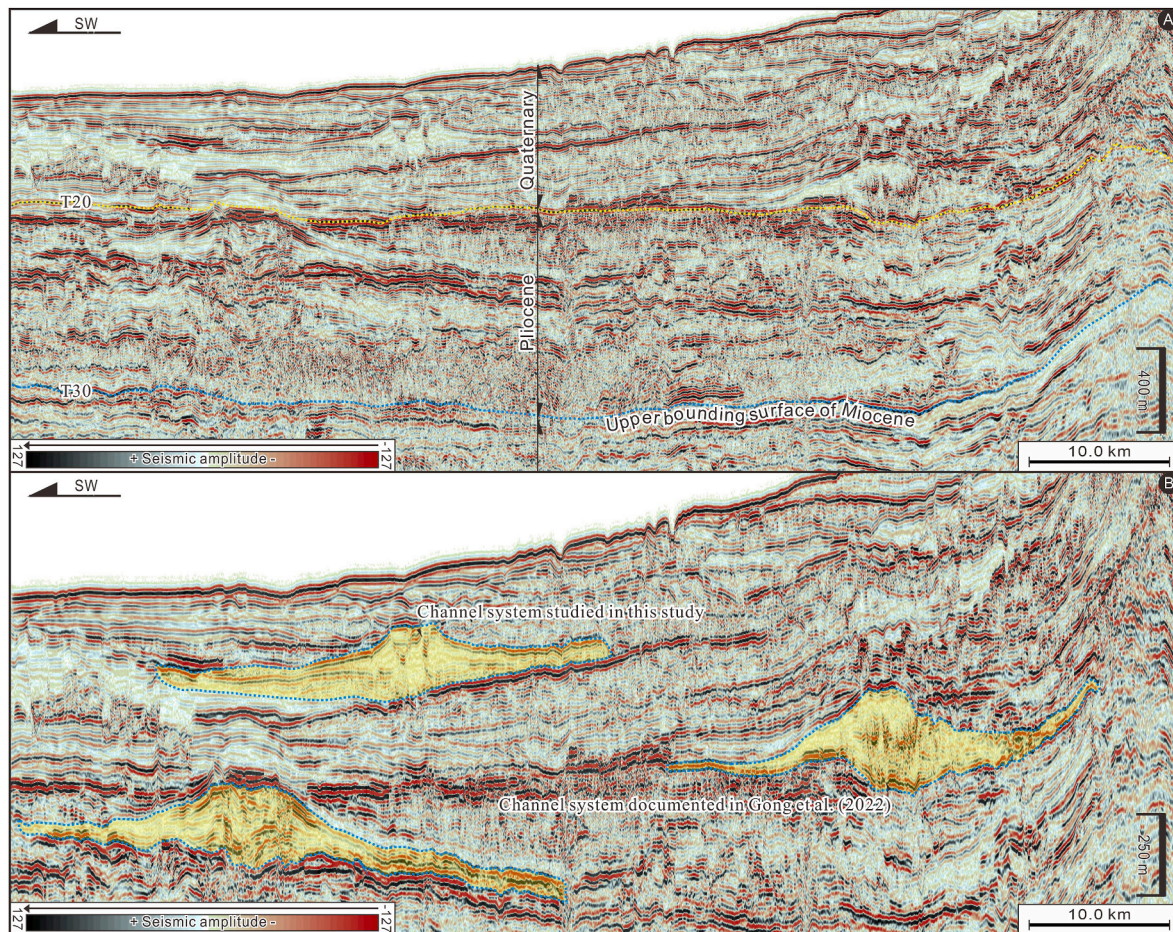


Fig. 2. Uninterpreted and interpreted regional 2D seismic profile (see Fig. 1A for line location) showing the regional occurrence of three channel-levee systems in the Pliocene-Quaternary succession of the Rakhine Basin. Note that only a single channel-levee system was active at a given interval of the geological time.

submarine fan system in the world, with a length of ca. 3000 km, a width of ca. 1000 km, a maximum thickness of up to 16.5 km below the Bangladesh shelf, and an area of up to $3 \times 10^6 \text{ km}^2$ (Curry et al., 2003; Yang and Kim, 2014). It was initiated by the collision of India with Asia and subsequent uplift of the Himalayan mountain range and Tibetan Plateau in the Middle Paleocene to Early Eocene (Curry et al., 2003). The Bengal Fan was fed by terrigenous clastic sediments eroded from the Himalayas, which have shed into the Bay of Bengal through the Ganges-Brahmaputra sediment-routing systems, with a sediment load of ca. $1.2 \times 10^9 \text{ t/year}$ (i.e., Earth's largest modern-day source-to-sink sediment-dispersal system) (Blum et al., 2018). The Bengal Fan represents the terminal sink of the world's largest source-to-sink systems (i.e., Ganges-Brahmaputra-Bengal sediment-routing systems) (Fig. 1A) (Blum et al., 2018; Pickering et al., 2020). The Bengal Fan can be classified as a fine-grained, mud-rich submarine fan system (Mattern, 2005), with sand content estimated to be less than 30%, as revealed by cores of the IODP Expedition 354 (Bergmann et al., 2020).

The formation and evolution of the Rakhine Basin in the north-eastern fringe of the upper Bengal subfan were related to the oblique convergence of the Indian and Burmese Plates and subsequent westward migration of the developing accretionary wedge (Indo-Burma Range) since the Paleocene (Ma et al., 2020; Zhou et al., 2020). The Rakhine Basin is a Tertiary foredeep basin, and was filled by Cretaceous-Quaternary deposits, with a maximum thickness of up to

12000 m (Yang and Kim, 2014; Ma et al., 2020; Zhou et al., 2020). The Neogene to Quaternary Rakhine Basin is dominated by sediment gravity-flow deposits consisting of fine massive sandstones, fine siltstones, and dark gray mudstones (Ma et al., 2020; Zhou et al., 2020).

Deepwater systems, including channel-levee systems, lobes and mass-transport complexes, developed during the Neogene to Quaternary (Yang and Kim, 2014; Ma et al., 2020; Zhou et al., 2020). Two basin-wide unconformities (i.e., T30 and T20) are recognized in the Pliocene-Quaternary succession of the Rakhine Basin (Fig. 2A) (Ma et al., 2020; Gong et al., 2022). T30 and T20 refer to the basal bounding surfaces of Pliocene and Quaternary, respectively (Fig. 2A) (see Ma et al., 2020 for a detailed seismic-well tie). The Quaternary interval is the shallowest and best-imaged stratal interval with seismically well-imaged channel-levee systems that are the focus of the present study (Fig. 2B).

3. Data and methodology

3.1. Three-dimensional (3D) seismic data

The primary data of this study consists of 3D seismic data, acquired from the Rakhine Basin by Chinnery Assets limited Company (polygon with solid outline in Fig. 1A). 3D seismic survey covers an area of ca. 1400 km^2 , with a water depth ranging from 1125 to 2025 m (Fig. 1B).

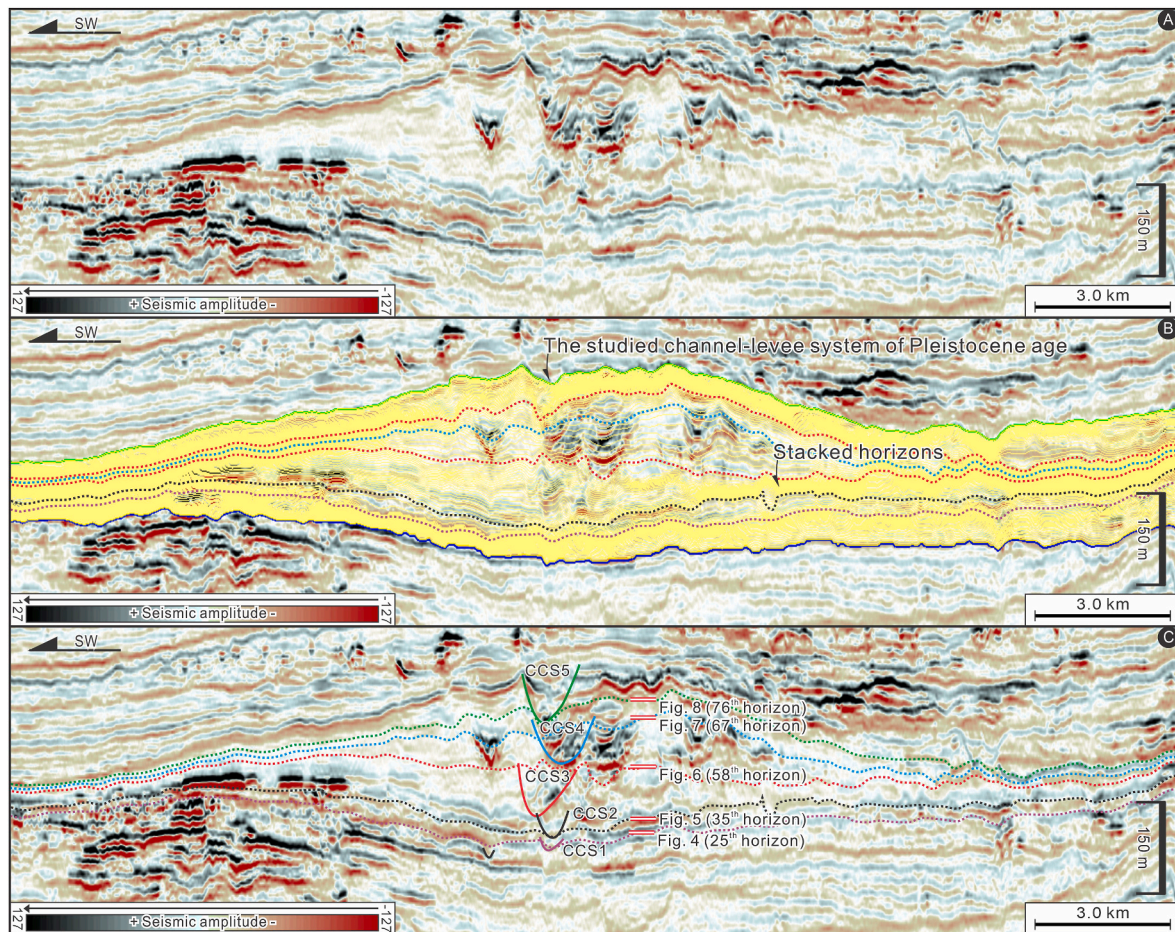


Fig. 3. Uninterpreted (A) and interpreted (B) seismic transects (see Fig. 1B for line location) illustrating horizon stack containing 100 surfaces (numbered 1 to 100 in chronological order). Note that upper and basal bounding surfaces of the shown channel-leeve system are used to constrain the PaleoScan geomodel of geological consistency for stratal slicing. (C) Seis profile showing stratigraphic positions of seismic attribute maps shown in Fig. 4–8. CCSs seen in seismic attribute maps of Fig. 4 (25th horizon), Fig. 5 (35th horizon), Fig. 6 (58th horizon), Fig. 7 (67th horizon), and Fig. 8 (76th horizon) are here referred to as CCS1, CCS2, CCS3, CCS4, and CCS5, respectively.

The 3D seismic data used in this study are in the time domain, have been processed with zero phase, and have a bin size spacing of 25 m (in-line) by 12.5 m (cross-line). They have a frequency bandwidth ranging from 10 to 55 Hz and a dominant frequency of 30 Hz for the study interval. 3D seismic data are tied to regional 2D seismic lines shown in Fig. 2. Both 2D and 3D seismic datasets have a sampling interval of 4 ms, and have been processed using a pre-stack hybrid migration algorithm. They are displayed using SEG positive standard polarity, where a positive reflection coefficient is represented by a central peak (black in color) (Fig. 2). They are displayed using a red-white-black color bar, where the low-impedance reservoir top is displayed as a trough (red in color) (Fig. 2). 3D seismic data were used to document morphometrics, architectures and evolution of Quaternary deep-water channels shown in Fig. 2.

3.2. Full-volume 3D seismic interpretation

The workflow for full-volume 3D seismic interpretation of the studied channels consists of: (1) defining and mapping upper and basal bounding surfaces of deep-water channel systems documented in this study (Fig. 3A); (2) creating horizon stack containing 100 surfaces using PaleoScan™ (Fig. 3A); and (3) integrating seismic attribute maps with

cross-sectional seismic transects to characterize morphometric attributes, architectures, and evolution of the studied submarine channel systems. We used two ways to reduce the uncertainties of automatic generation of horizon stacks from 3D seismic datasets. Firstly, we carefully mapped and manually picked the same stratigraphic levels of both basal and upper bounding surfaces of the documented channel systems (green and blue solid lines in Fig. 3B) throughout the whole study area. Secondly, these two horizons were taken as the chronostratigraphic markers and frameworks for the creation of auto-tracked channel surfaces, using PaleoScan™ (cf. Paumard et al., 2020). Horizon patches in PaleoScan™ Model-Grid were computed and constrained by basal and upper bounding surfaces of the documented channel systems. They are also editable and polarity-consistent, either in peak, trough, zero-crossing, or inflection points (Paumard et al., 2019, 2020). Horizon stack with 100 auto-tracked channel surfaces was numbered 1 through 100 in a chronological order (Fig. 3B). Five representative channel surfaces (25th, 35th, 58th, 67th, and 76th horizons in Fig. 3C) were selected to establish seismic attributes maps.

Seismic attribute volumes were computed from 3D seismic volume, including spectral decomposition and the root mean square amplitude (RMS) (Figs. 4–8). Spectral decomposition transforms seismic data into the frequency domain (Othman et al., 2016; Howlett et al., 2021). In this

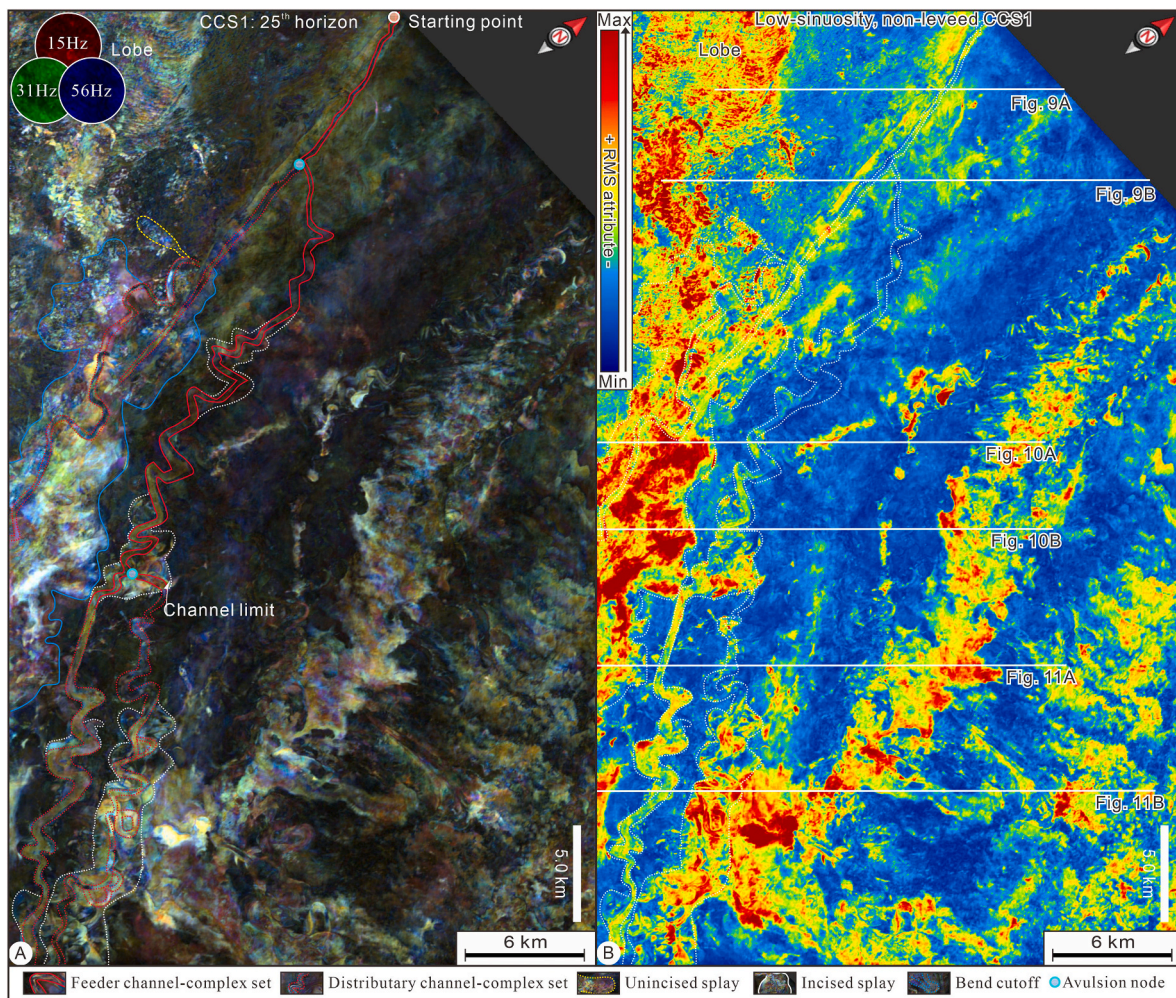


Fig. 4. RGB spectral decomposition-attribute and RMS amplitude maps taken along the 25th PaleoScan horizon (see Fig. 3C for their stratigraphic position) showing the representative seismic geomorphology of erosional non-leveed CCS1 and its associated architectural elements. Please refer to Fig. S1 for uninterpreted attribute maps shown in this figure.

study, three different frequencies centered at 15 Hz, 31 Hz, and 56 Hz were mapped on 100 surfaces from horizon stack shown in Fig. 3. These three different frequencies of 15 Hz, 31 Hz, and 56 Hz were, respectively, assigned to red, green, and blue on RGB color blending viewer of PaleoScan™ (Figs. 4–8). RMS attributes calculate the square root of the sum of the time-domain energy, and therefore offer the enhanced visualization of the geomorphology of small-scale architectural elements (Posamentier et al., 2022).

3.3. Morphometric attributes

This study is based mainly on commercially acquired 3D seismic data, and the smallest channel form resolvable on seismic reflection data is channel-complex set (CCS) (Mayall et al., 2006, 2010; Edwards et al., 2017; Gong et al., 2021; Bouchakour et al., 2022, 2023). Thus, this study focuses at the scale of CCSs.

Morphometric attributes of the studied CCSs include width of CCS (W), thickness of CCS (T), aspect ratio of CCS (W/T), cross-sectional area of CCS (C_a), and sinuosity of CCS (S_i). Specifically, (i) W is measured as the maximum horizontal distance between channel walls; (ii) T is considered to be the maximum vertical distance from the channel base to the top of the channel banks; (iii) W/T is defined as CCS width divided

by CCS thickness; (iv) C_a refers to the cross-sectional area measured perpendicular to the direction of CCS (see also Qin et al., 2020); and (v) S_i is defined as the ratio of the centerline length (thalweg length) to the corresponding straight-line distance (straight path) of CCS (Bridge, 2003). Measurements of W , T , C_a , and S_i were carried out at the increment of 1.25 km (along the centerline of the studied CCSs) away from the starting points marked as white dots in Figs. 4–8 (0 km along-channel distance), resulting in 37 data points for each of the five studied CCSs. Depth measurements of these morphometric attributes were estimated, using 2000 m/s for the shallow siliciclastics in the study interval of interest and 1500 m/s for the seawater.

4. Architectural elements of the studied channel systems

Four main types of architectural elements are identified in the study area, based on RMS amplitude and RGB spectral decomposition attribute maps integrated with seismic profiles (Figs. 4–8; Table 1).

4.1. Feeder and distributary channel-complex set

This architectural element is distinguished in cross-section by concave-up scours filled by moderate-to high-amplitude discontinuous

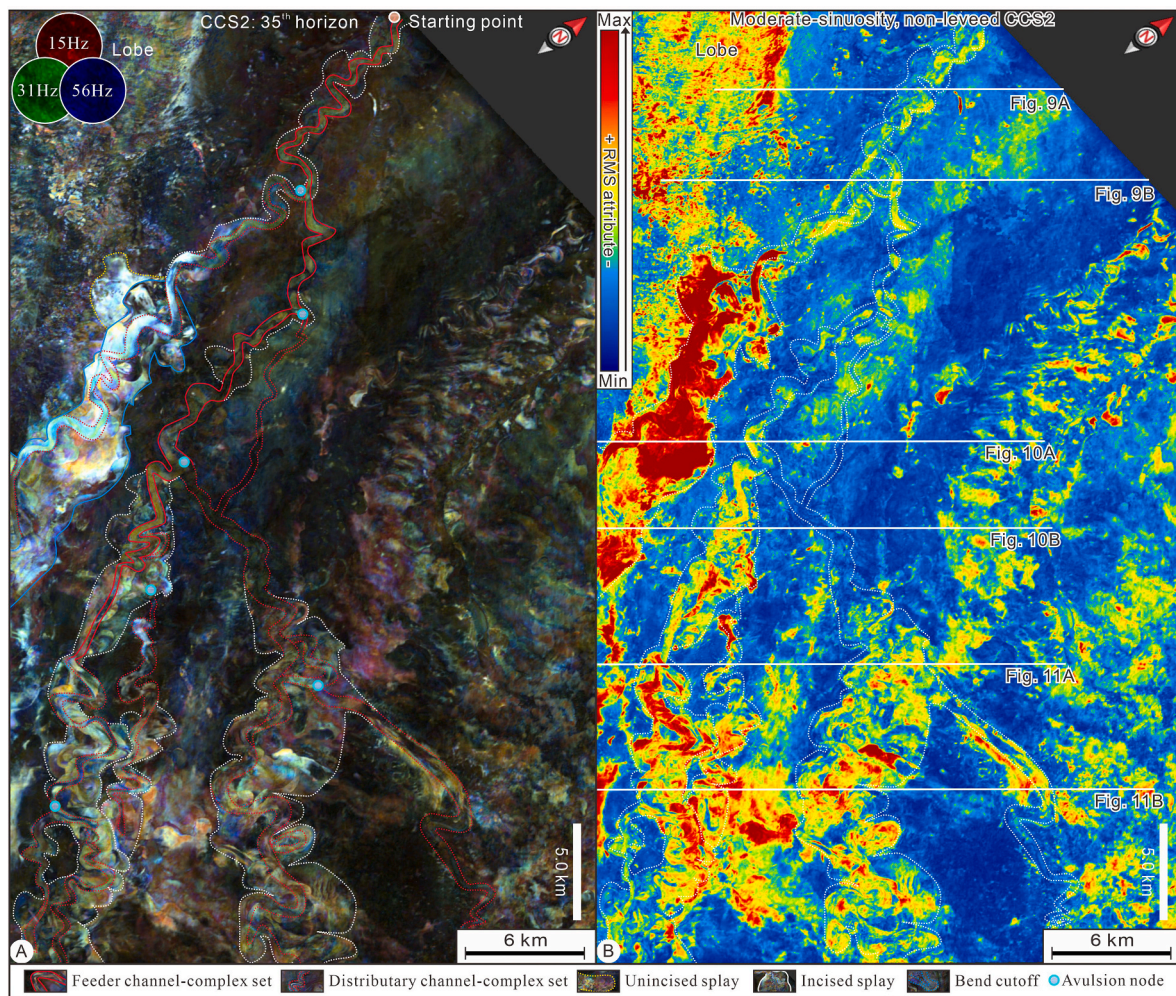


Fig. 5. RGB spectral decomposition-attribute and RMS amplitude maps extracted from the 35th PaleoScan horizon (see Fig. 3C for their stratigraphic position) illustrating the representative seismic geomorphology of erosional non-leveed CCS2 and its associated architectural elements. Please refer to Fig. S2 for uninterpreted attribute maps shown in this figure.

to chaotic reflectors (Figs. 9–11; Table 1). It occurs in seismic attribute maps as narrow and sinuous fairways extending tens of kilometers (Figs. 4–8), and exhibits two markedly different patterns in cross-sections (Figs. 9–11; Table 1). The first seismic-reflection pattern occurs in upstream segments of the documented channels (Figs. 4–8), and is characterized by channel-shaped, high-amplitude discontinuous reflections flanked by low-to moderate-amplitude and continuous reflections, forming a typical “gull-wing” seismic signature (Figs. 9 and 10). The second seismic-reflection pattern occurs preferentially in the downstream segments of the documented channel systems (Figs. 4–8). It is expressed as channel-shaped, high-amplitude discontinuous reflections with a lack of seismic resolvable levees (Fig. 11).

The two patterns described above share a similar seismic geomorphology in many other studies that have labelled them as submarine channels (e.g., Mayall et al., 2006; Janocko et al., 2013; Oluboyo et al., 2014; Gong et al., 2021; Howlett et al., 2021; Tek et al., 2021). Similar to Doughty-Jones et al. (2017), Howlett et al. (2021), and Tek et al. (2021), we interpret the areally larger submarine channels as feeder CCSs flanked by “gull-wing” levees (Table 1). These feeder CCSs are linked downstream to areally smaller submarine channels that can be best considered as distributary CCSs (i.e., streams branching off and flowing

away from a main feeder channel) (Table 1) (e.g., Doughty-Jones et al., 2017; Howlett et al., 2021).

4.2. Bend cutoffs

This architectural element associated with the documented channel systems appears in seismic sections as lenticular, high-amplitude discontinuous reflections, and is blanketed wholly by low-amplitude reflections (cool color-shaded lens in Fig. 10; Table 1). It is manifested in attribute maps as cutoff meander loops of high-sinuosity leveed channels (i.e., neck cutoffs or bend cutoffs) (Figs. 6–8; Table 1). These elements are seen to occur preferentially along the upstream segments of the documented channel systems imaged in Figs. 6–8.

Posamentier and Kolla (2003) and Janocko et al. (2013) have suggested that cutoff meander loops of high-sinuosity, leveed channels can be considered as bend cutoffs. We, therefore, interpret the above-mentioned seismic reflection patterns as the same architectural elements (i.e., bend cutoffs) (Figs. 6–8). The documented bend cutoffs represent the abandoned channel forms that preserve the last stage of meandering, and are a few kilometers wide, and are highly sinuous (Figs. 6–8).

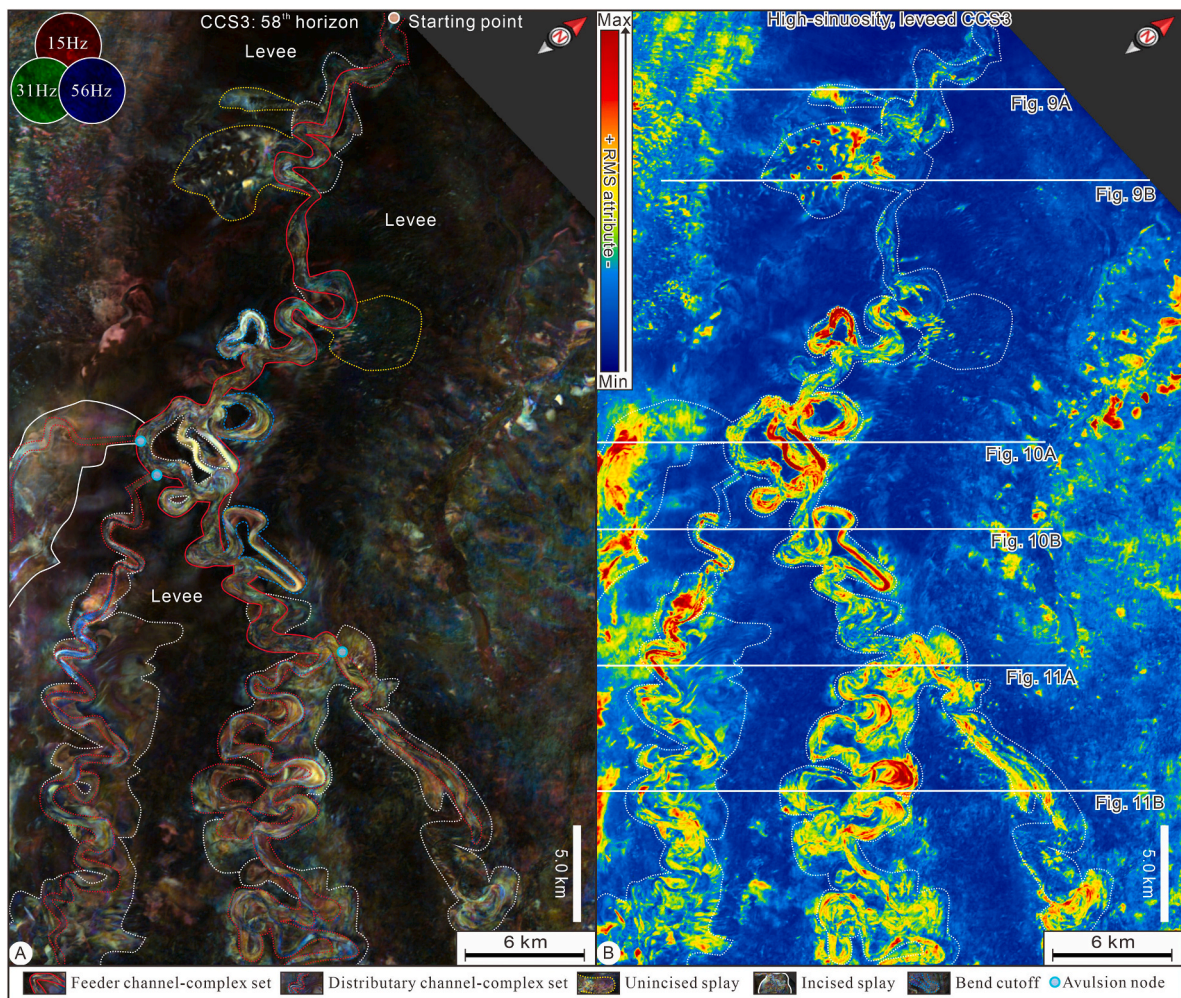


Fig. 6. RGB spectral decomposition-attribute and RMS amplitude maps extracted from the 58th PaleoScan horizon (see Fig. 3C for their stratigraphic position) visualizing the representative seismic geomorphology of graded CCS3 and its associated architectural elements. Please refer to Fig. S3 for uninterpreted attribute maps shown in this figure.

4.3. Levees

This architectural element associated with the documented channel systems is composed of low-amplitude, continuous seismic reflections showing wedge-shaped cross-sectional geometries (Figs. 9–11; Table 1). It is seen to occur along both sides of the studied channels, and decreases in thickness away from the channel axis (Figs. 9–11; Table 1). In plan view, this architectural element is imaged on RGB spectral decomposition-attribute maps as areally extensive (i.e., 10s–100 s km²), dark colored accumulations and on RMS amplitude images as blue, low RMS amplitude accumulations (Figs. 4–8).

Similar seismic character is widely referred to overbank levees by many authors (e.g., Posamentier and Kolla, 2003; Deptuck et al., 2003, 2007; Oluboyo et al., 2014; Oluboyo et al., 2014; Hansen et al., 2017; Howlett et al., 2021; Bouchakour et al., 2022). The studied levees were formed when turbidity currents exceed the confinement height of the documented CCS, thereby spilling and delivering fine-grained sediments onto channel overbank environments (Hansen et al., 2015, 2017). They

are a few to several kilometers in width, and are tens to a few hundreds of meters in height (Figs. 9 and 10).

4.4. Incised and unincised crevasse splays

This architectural element associated with the documented channel system is made up of wedge-shaped, moderate-to high-amplitude seismic reflections (yellow color-shaded areas in Figs. 9 and 10A; Table 1). It thins and downlaps towards its fringes (Figs. 9 and 10A; Table 1). This architectural element occurs in attribute maps as unconfined lobate features that often derive from sharp bends of high-sinuosity channels (i.e., feeder CCS) (Figs. 4–8; Table 1).

Based on seismic characteristics and planform distribution patterns, wedge-shaped, moderate-to high-amplitude seismic reflections with lobate morphology can be interpreted as crevasse-splay elements (Posamentier and Kolla, 2003; Janocko et al., 2013; Maier et al., 2013; Lowe et al., 2019) (Figs. 9 and 10A; Table 1). Two main types of crevasse splays are recognized, including incised and unincised splays. The

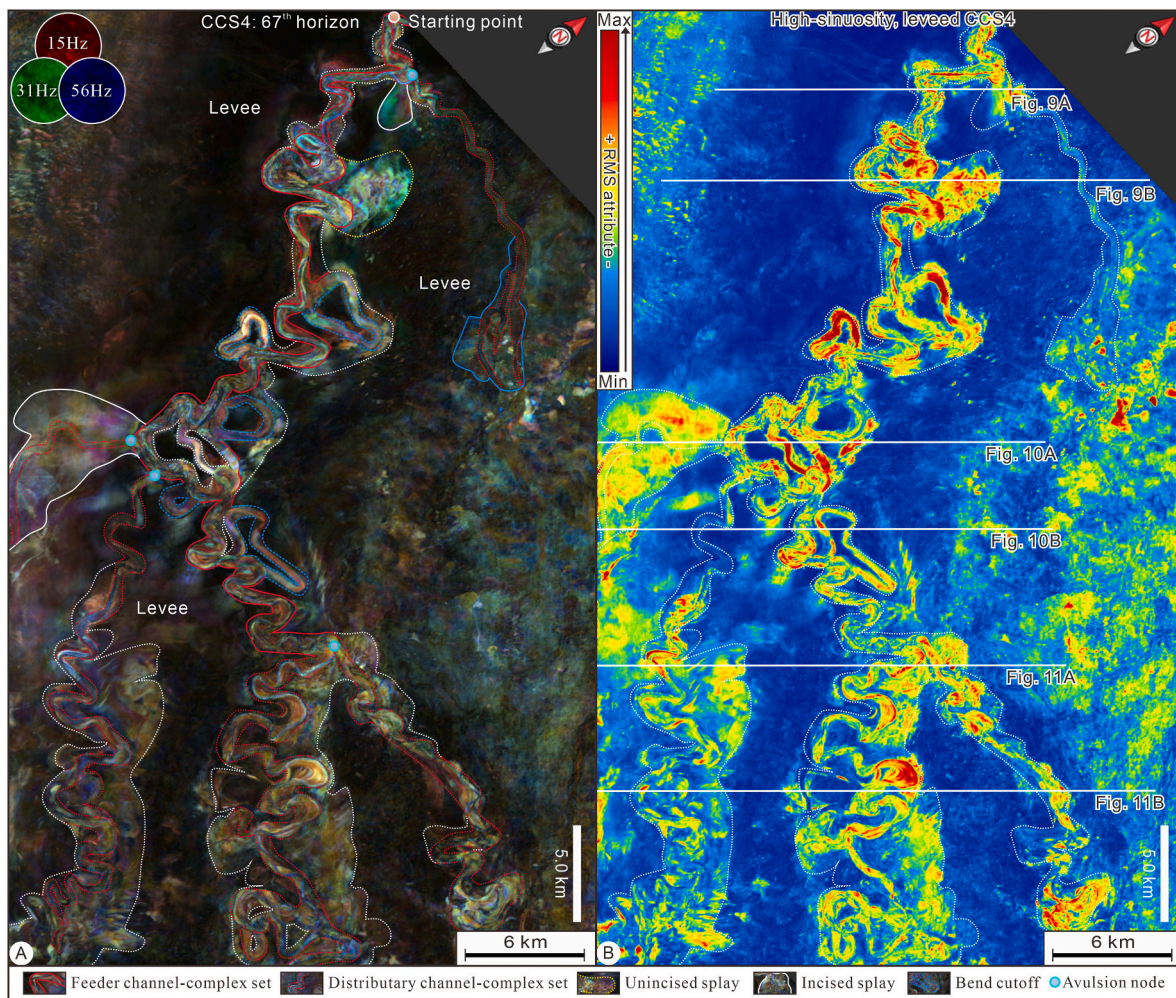


Fig. 7. RGB spectral decomposition-attribute and RMS amplitude maps extracted from the 67th PaleoScan horizon (see Fig. 3C for their stratigraphic position) delineating the representative seismic geomorphology of aggradational leveed CCS4 and its associated architectural elements. Please refer to Fig. S4 for uninterpreted attribute maps shown in this figure.

former is typically incised by small distributary CCSs, whereas the later is devoid of any channel incision (Fig. 6A to 8A). The documented crevasse splays are a few to several kilometers in width, and a few to several tens of meters in height (Figs. 6–9, and 10A).

5. Architecture and morphometrics of channel-complex sets

The entire submarine channel system as documented in this study contains five main channel-complex sets (CCS1 to CCS5), each of which records a specific morphology and stratigraphic architecture, as discussed below.

5.1. Geomorphology and architecture of CCS1

CCS1 is well illustrated by RGB spectral decomposition-attribute and RMS amplitude maps extracted from the 25th surface of the PaleoScan horizon stack (Figs. 3 and 4). Morphologically, CCS1 has width (W) of 92–197 m (averaging 139 m) (Figs. 12 and 13A), thickness (T) of 12–22 m (averaging 18 m) (Fig. 12A and 13B), aspect ratio (W/T) of

4.88–14.20 (averaging 7.32) (Fig. 13C), cross-sectional area (C_a) of 1013–6479 m² (averaging 2613 m²) (Fig. 12B and 13D), and a sinuosity (S_i) ranging from 1.00 to 2.02 with a mean value of 1.02 (Fig. 14A).

Stratigraphically, CCS1 is located at the lowermost stratigraphic level of the studied seismic interval (Figs. 3 and 9 to 11). The chronologically oldest CCS1 is not flanked by seismically resolvable levees, crevasse splays or bend cutoffs (Figs. 9–11; Table 2). In map view, CCS1 is characterized by a lack of coeval crevasse splays and/or bend cutoffs (Fig. 4; Table 2), but contains two avulsion nodes (blue dots in Fig. 4).

5.2. Geomorphology and architecture of CCS2

CCS2 is visualized by RGB spectral decomposition-attribute and RMS amplitude maps extracted from the 35th surface of the PaleoScan horizon stack (Figs. 3 and 5). Morphologically, CCS2 has W of 133–266 m (averaging 188 m) (Figs. 12 and 13A), T of 17–34 m (averaging 24 m) (Fig. 12A and 13B), W/T of 5.83–10.46 (averaging 7.85) (Fig. 13C), C_a of 2146–6479 m² (averaging 3655 m²) (Fig. 12B and 13D), and S_i of 1.00–2.11 (averaging 1.30) (Fig. 14A).

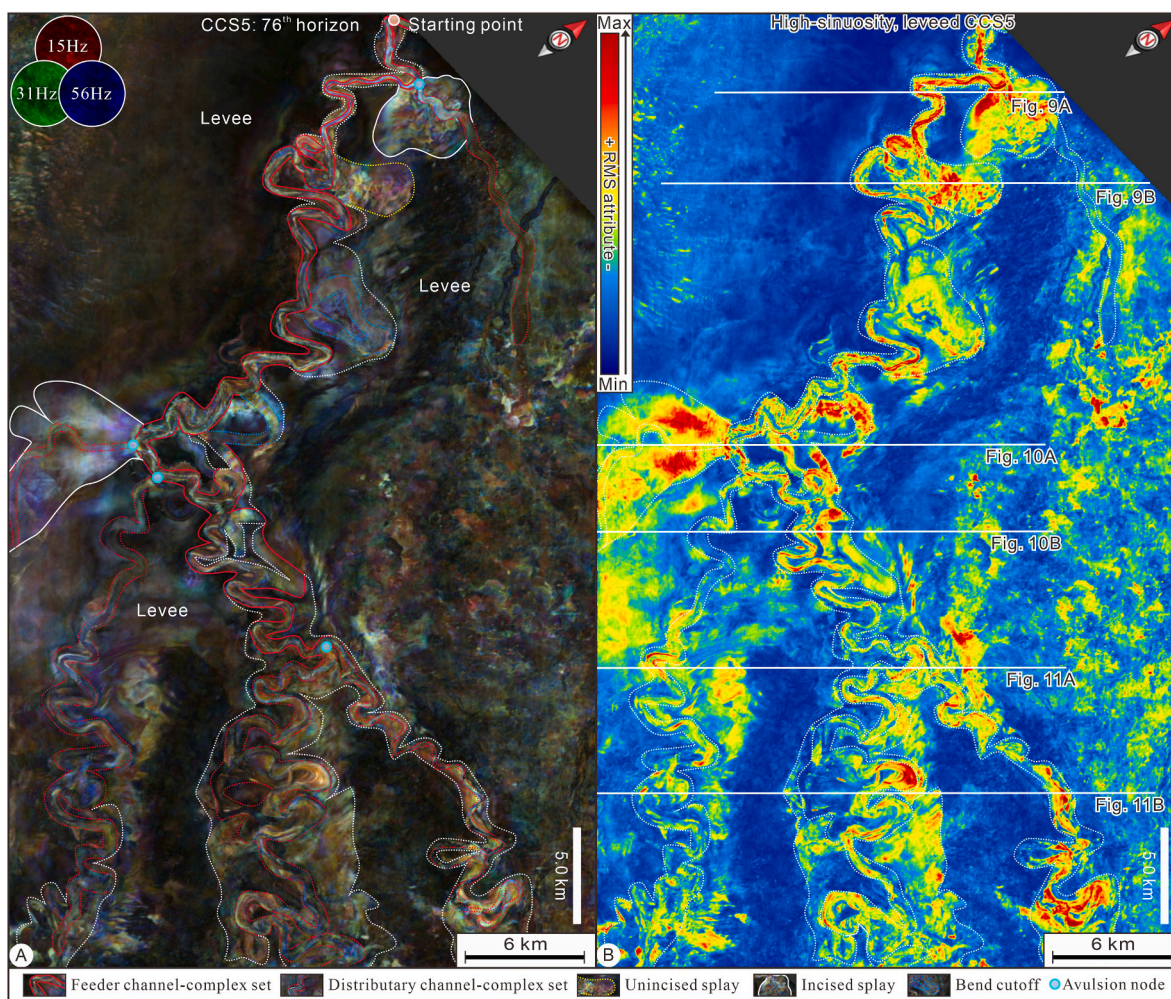
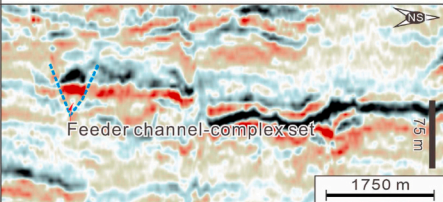
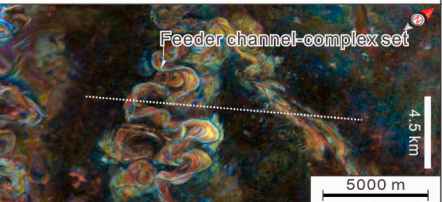
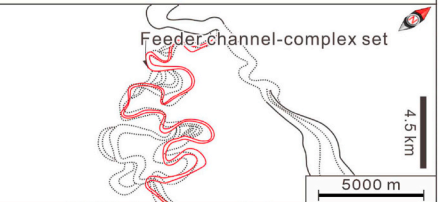
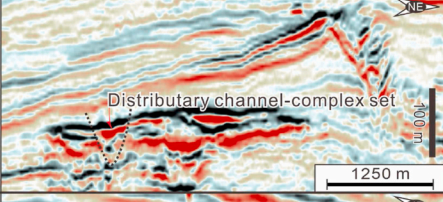
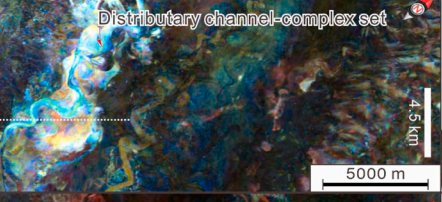
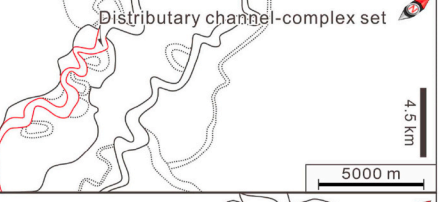
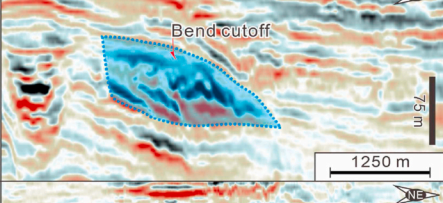

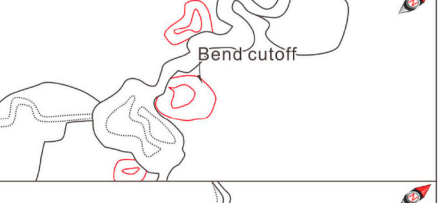
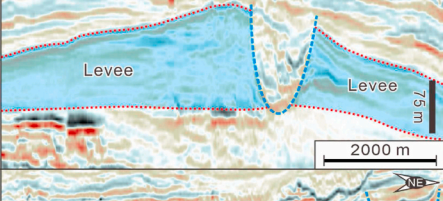
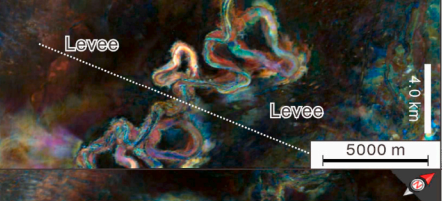
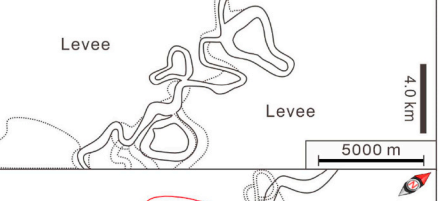
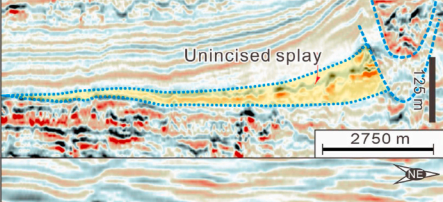
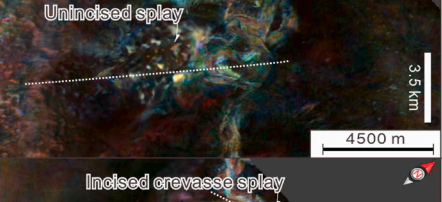
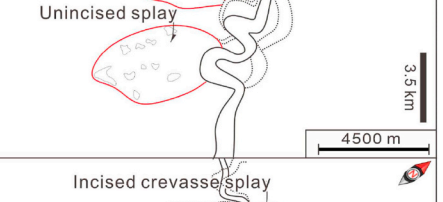





Fig. 8. RGB spectral decomposition-attribute and RMS amplitude maps extracted from the 76th PaleoScan horizon (see Fig. 3C for their stratigraphic position) illustrating the representative seismic geomorphology of aggradational leveed CCS5 and its associated architectural elements. Please refer to Fig. S5 for uninterpreted attribute maps shown in this figure.

Table 1
A summary of architectural elements associated with the documented channel systems as observed in seismic sections and on RGB spectral decomposition-attribute maps.

	Cross-sectional seismic manifestations	Planform seismic geomorphology	Planform line drawings
Feeder channel-complex set			
Distributary channel-complex set			
Bend cutoff			
Levee			
Unincised splay			
Incised splay			

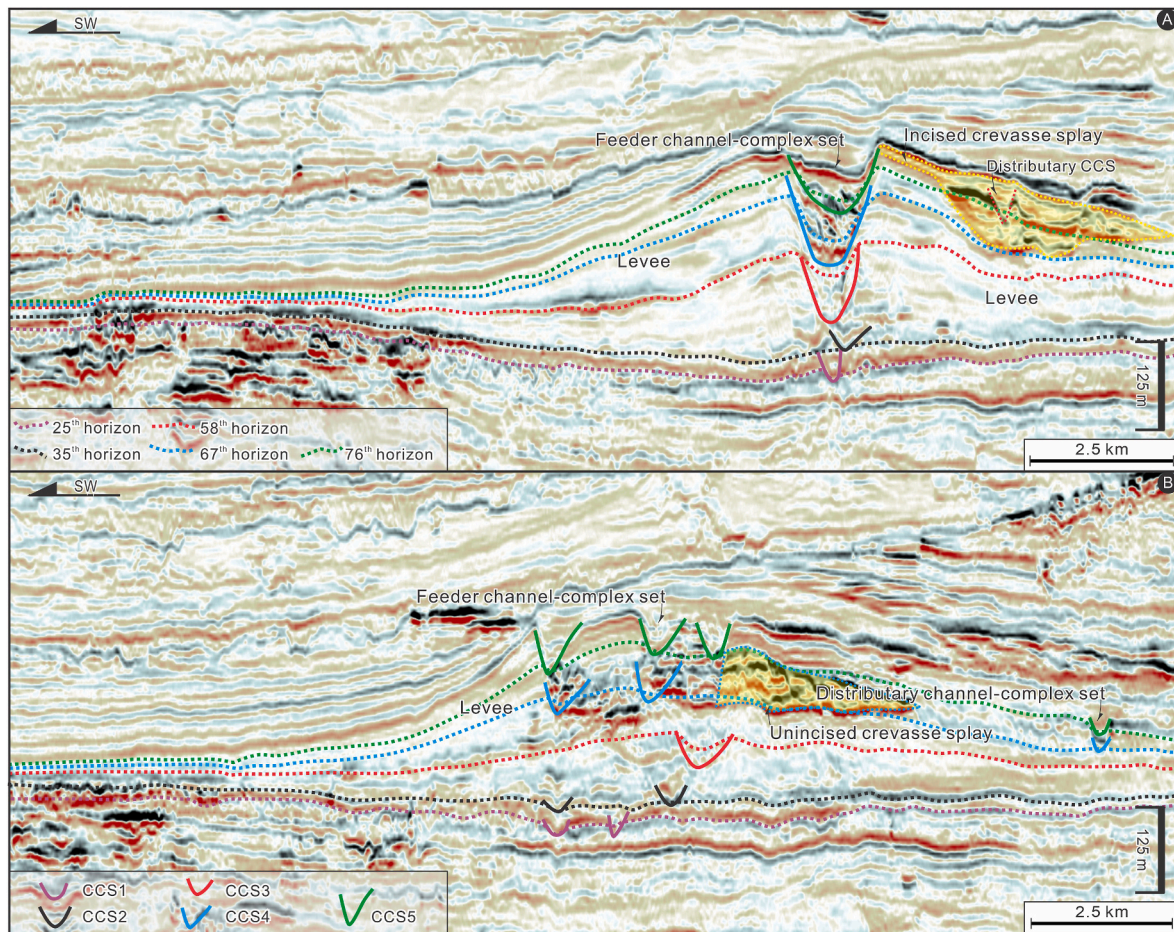


Fig. 9. Seismic profiles along the depositional dip (see Fig. 4–8 for their map-view locations) offering seismic reflection patterns of the documented CCS1 to CCS5 and their associated architectural elements (e.g., feeder CCSs, levees, distributary CCSs, incised crevasse splays, and unincised crevasse splays). Please refer to Fig. S6 for uninterpreted seismic profiles shown in this figure.

Stratigraphically, CCS2 occurs above CCS1 and is located at the lower stratigraphic level of the studied channel system (Figs. 3 and 9 to 11). Similar to CCS1, CCS2 is also characterized by a lack of seismically resolvable levees and other overbank elements such as crevasse splays and/or bend cutoffs (Figs. 9–11). In map view, CCS2 is manifested in seismic attribute maps as moderate-sinuosity trains of scours, and contains six avulsion nodes along its entire length (Fig. 5; Table 2).

5.3. Geomorphology and architecture of CCS3

CCS3 is documented by RGB spectral decomposition-attribute and RMS amplitude maps extracted from the 58th surface of the PaleoScan horizon stack (Figs. 3 and 6). Morphologically, CCS3 has W of 461–1102 m (averaging 745 m) (Figs. 12 and 13A), T of 49–128 m (averaging 89 m) (Fig. 12A and 13B) (Fig. 12A and 13B), W/T of 6.76–11.22 (averaging 8.56) (Fig. 13C), C_a of 18057–88027 m^2 (averaging 49183 m^2) (Fig. 12B and 13D), and S_i of 1.00–3.69 (averaging 1.44) (Fig. 14A).

Stratigraphically, CCS3 is located in the middle stratigraphic level of the studied channel system (Figs. 3 and 9 to 11). In marked contrast to CCS1 and CCS2, CCS3 is flanked by concomitant levees (Figs. 9–11; Table 2); which appear in seismic attribute maps as uniform to patchy low-amplitude zones on both sides of the CCS3 (Fig. 6). In map view,

CCS3 is accompanied by crevasse splays and bend cutoffs, and contains three avulsion nodes along its entire length (Fig. 6; Table 2).

5.4. Geomorphology and architecture of CCS4

CCS4 is illustrated by RGB spectral decomposition-attributes and RMS amplitude maps extracted from the 67th surface of the PaleoScan horizon stack (Figs. 3 and 7). Morphologically, ranges in W , T , W/T , C_a , and S_i of CCS4 are, respectively, 203–757 m (averaging 476 m) (Figs. 12, 13A) and 16–93 m (averaging 57 m) (Fig. 12A, 13B) and 5.75–19.07 (averaging 9.25) (Figs. 13C), 2882–42268 m^2 (averaging 22679 m^2) (Fig. 12B, 13D) and 1.01 to 4.00 (averaging 1.54) (Fig. 14A).

Stratigraphically, CCS4 is located just below the uppermost part of the studied system (Figs. 3 and 9 to 11). In marked contrast to CCS1 and CCS2, CCS4 is flanked by areally extensive levees (Figs. 9 and 10), which are imaged in seismic attribute maps as regionally extensive, uniform to patchy high-amplitude zones on both flanks of CCS4 (Fig. 7). However, these levees are areally larger than levees asymmetrically developed along both flanks of CCS3. In map view, CCS4 is flanked by both incised and unincised crevasse splays, and is characterized by frequent occurrence of channel bend cutoffs and prominent avulsions (i.e., four avulsion nodes) (Fig. 7; Table 2).

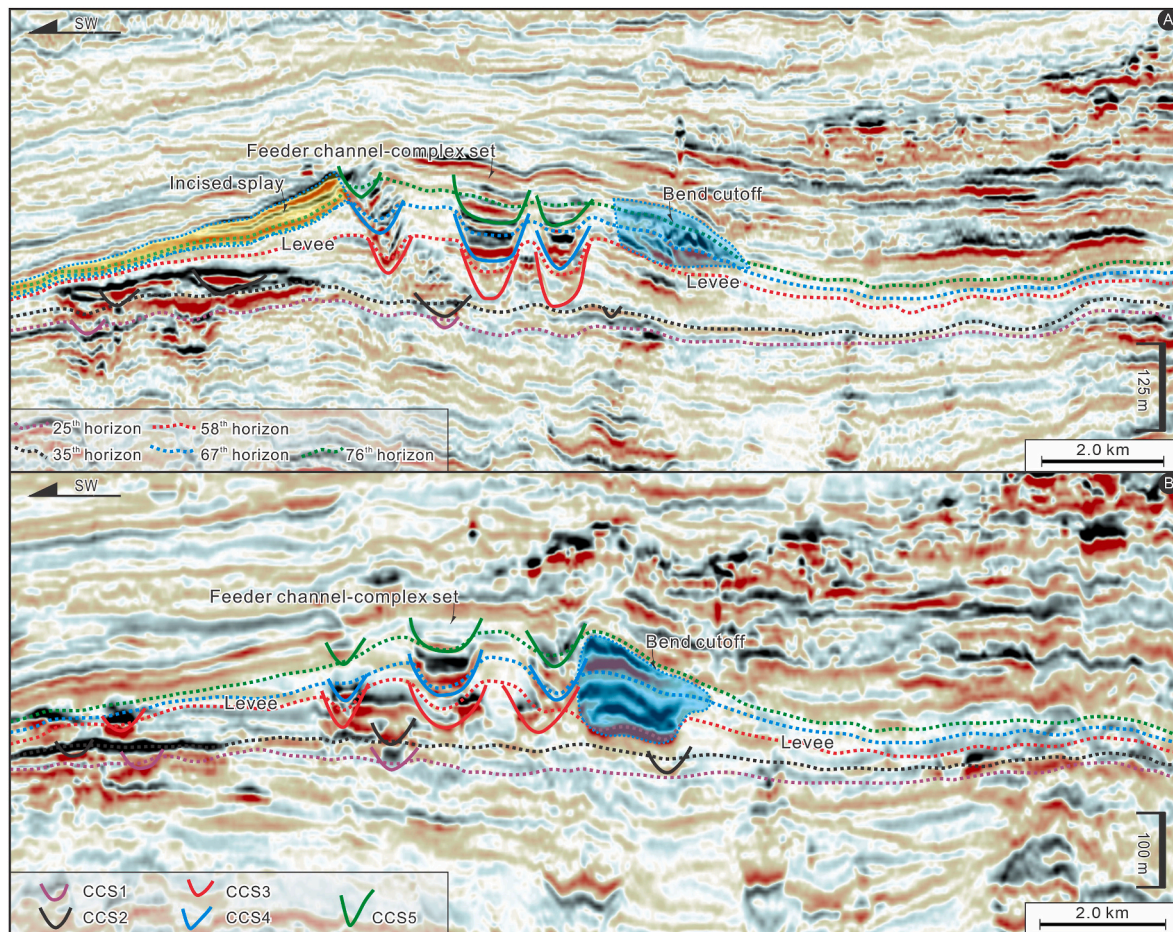


Fig. 10. Depositional dip-oriented seismic traverses (see Fig. 4–8 for their map-view locations) showing cross-sectional seismic manifestations of the documented CCS1 to CCS5 and their associated architectural elements (e.g., feeder CCSs, incised splay, levees, and bend cutoffs). Please refer to Fig. S7 for uninterpreted seismic profiles shown in this figure.

5.5. Geomorphology and architecture of CCS5

CCS5 is well delineated by RGB spectral decomposition-attributes and RMS amplitude maps extracted from the 76th surface of the PaleoScan horizon stack (Figs. 3 and 8). Morphologically, CCS5 exhibits W of 310–772 m (averaging 476 m) (Figs. 12 and 13A), T of 24–89 m (averaging 56 m) (Fig. 12A and 13B), W/T of 6.06–15.94 (averaging 9.05) (Fig. 13C), and C_a of 5587–49901 m² (averaging 21257 m²) (Fig. 12B and 13D); and is characterized by a high S_i of 1.01–3.88, with a mean value of 1.64 (Fig. 14A).

Stratigraphically, CCS5 is located at topmost part of the studied channel succession (Figs. 3 and 9 to 11). Similar to CCS4, CCS5 is also flanked by areally extensive levees (Figs. 9 and 10; Table 2), and is therefore highly aggradational and strongly levee confined. In map view, CCS5 is accompanied by frequent occurrence of crevasse splays and bend cutoffs, and is characterized by prominent development of avulsions (i.e., four avulsion nodes) (Fig. 8; Table 2).

6. The types and evolution of the studied channel-complex sets

The analysis of morphometrics and architectures of the successive

channel-complex sets (CCSs) of CCS1, CCS2, CCS3, CCS4, and CCS5 suggests a differentiation of three types of CCSs, as discussed below.

6.1. The types of the documented CCSs and their characteristics

A statistical comparison of W , T and C_a among CCS1 to CCS5 suggests CCS1 and CCS2 to be statistically distinctive from the other examples (Figs. 12, 14B and 14C, and 14D). As shown in Figs. 12, 14B and 14C, and 14D, CCS1 and CCS2 are characterized by the lowest values of these variables (represented by W of 89–266 m with mean value of 153 m (Fig. 14B), T of 12–34 m with mean value of 20 m (Fig. 14C), and by C_a of 1013–6479 m² with mean value of 2613 m² (Fig. 14D; Table 3). Stratigraphically, CCS1 and CCS2 are stratigraphically expressed as V- or U-shaped, initial erosional conduits capable of eroding the pre-channel substrate (Figs. 9–11; Table 2), which, in turn, most likely fostered negative accommodation below the original equilibrium profile and its resultant erosional CCS (Kneller, 2003). Moreover, they are stratigraphically expressed as purely erosional features imaged as channel-shaped scours with no evidence of concomitant levees, and have straight to low-sinuosity fairways and low aspect ratios (Figs. 9–11; Table 2), all of which are compatible with characteristic features of

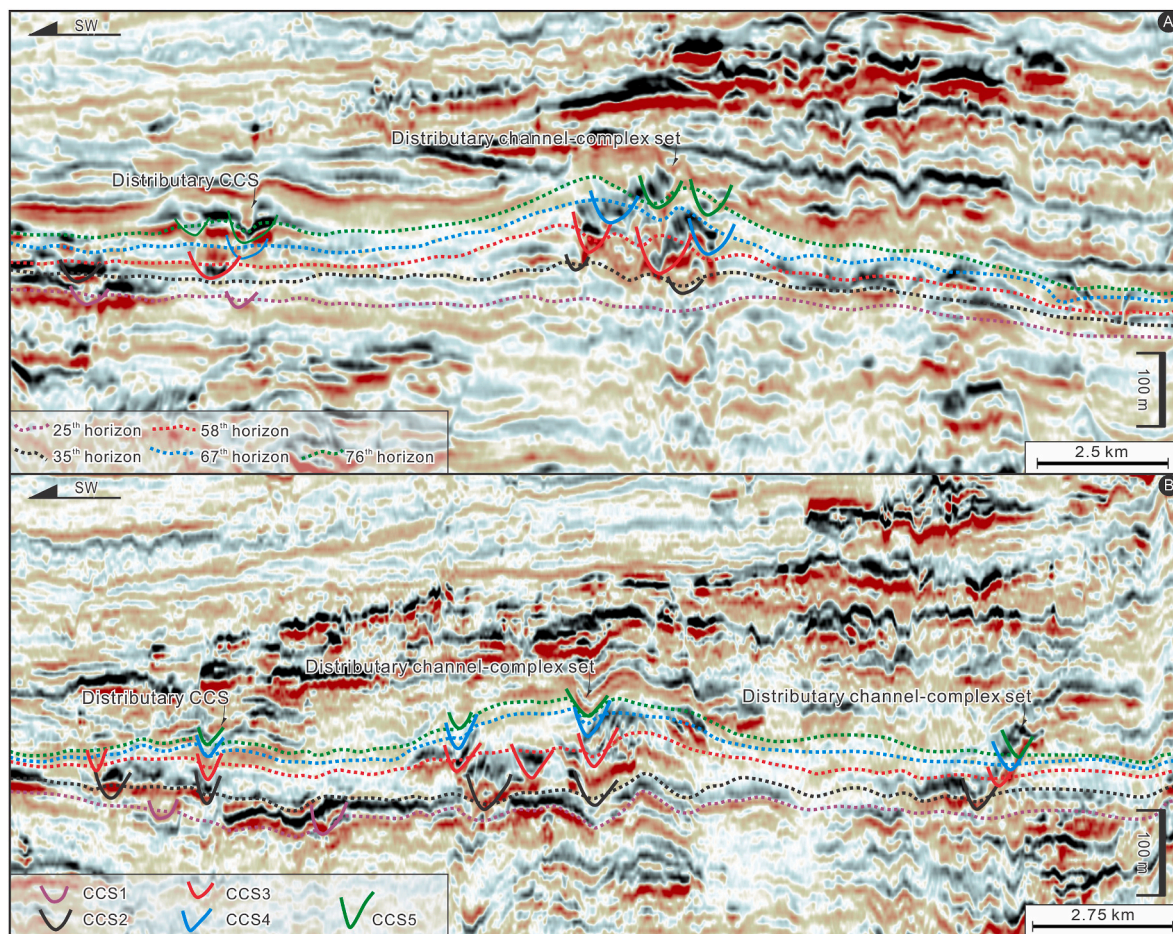


Fig. 11. Depositional dip-oriented seismic transects (see Fig. 4–8 for their map-view locations) showing cross-sectional seismic manifestations of the documented CCS1 to CCS5 (i.e., distributary CCSs). Please refer to Fig. S8 for uninterpreted seismic profiles shown in this figure.

erosional CCS documented by Kneller (2003) and Janocko et al. (2013). A lack of concomitant levees suggests a further reinterpretation of these erosional CCSs to be erosional non-leveed CCSs.

A statistical comparison in W , T and C_a among CCS1 to CCS5 shows CCS3 to be statistically distinctive from the other two types of CCSs (Figs. 12, 14B and 14C, and 14D). As shown in Figs. 12, 14B and 14C, and 14D, CCS3 is characterized by the highest values of these three parameters (represented by W of 461–1102 m with mean value of 745 m (Fig. 14B), T of 49–128 m with mean value of 89 m (Fig. 14C), and by C_a of 18057–88027 m² with mean value of 49183 m² (Fig. 14D), suggesting that CCS3 tend to be widest, deepest, and areally largest (Table 3). Stratigraphically, CCS3 is accompanied by crevasse splays and bend cutoffs, and is characterized by abundant lateral migration without significant channel-floor aggradation (Figs. 9–11; Table 2). The abundant lateral migration reflects little or no possibility for the documented CCS3 to aggrade, nor the tendency to erode (Kneller, 2003). Such processes, in turn, forced CCS3 to migrate laterally at the elevation of the equilibrium profile (Kneller, 2003), giving rise to graded CCSs (Kneller, 2003). Moreover, CCS3 are characterized by abrupt lateral offset of sinuous channel fairways, downstream sweep of meander-bends, and bend cutoffs (Figs. 9–11; Table 2), all of which are wholly compatible with the overall characteristics of graded CCSs (i.e., abundant lateral

migration without significant channel-floor aggradation and the occurrence of bend cutoffs and lateral-accretion features) (Kneller, 2003).

A statistical comparison in W , T and C_a among CCS1 to CCS5 suggests that CCS4 and CCS5 have intermediate values of these parameters (represented by W of 203–772 m with mean value of 476 m (Fig. 14B), T of 16–93 m with mean value of 56 m (Fig. 14C), and by C_a of 2882–49901 m² with mean value of 21968 m² (Fig. 14D), suggesting that CCS4 and CCS5 tend to be wider, deeper, and areally larger, as compared with CCS1 and CCS2 (Table 3). CCS4 and CCS5 are, therefore, statistically distinctive from erosional non-leveed CCSs of CCS1 and graded CCSs of CCS3 (Figs. 12, 14B and 14C, and 14D). Stratigraphically, CCS4 and CCS5 are highly aggradational, and strongly confined by levees, and have persistently accreted in a vertical direction through time (Figs. 9–11; Table 2), which, in turn, fostered new accommodation above the original equilibrium profile and its resultant aggradational leveed CCSs (Kneller, 2003). Moreover, CCS4 and CCS5 are imaged as single, well-defined, highly sinuous threads that migrated rather little, or commonly remain more or less fixed in position as they aggraded (Figs. 4 and 5, 9 to 11). These two lines of observations of CCS4 and CCS5 are wholly compatible with the overall characteristics of aggradational leveed CCSs (i.e., aggradational succession of leveed, sinuous CCSs) (Kneller, 2003; Janocko et al., 2013). The close

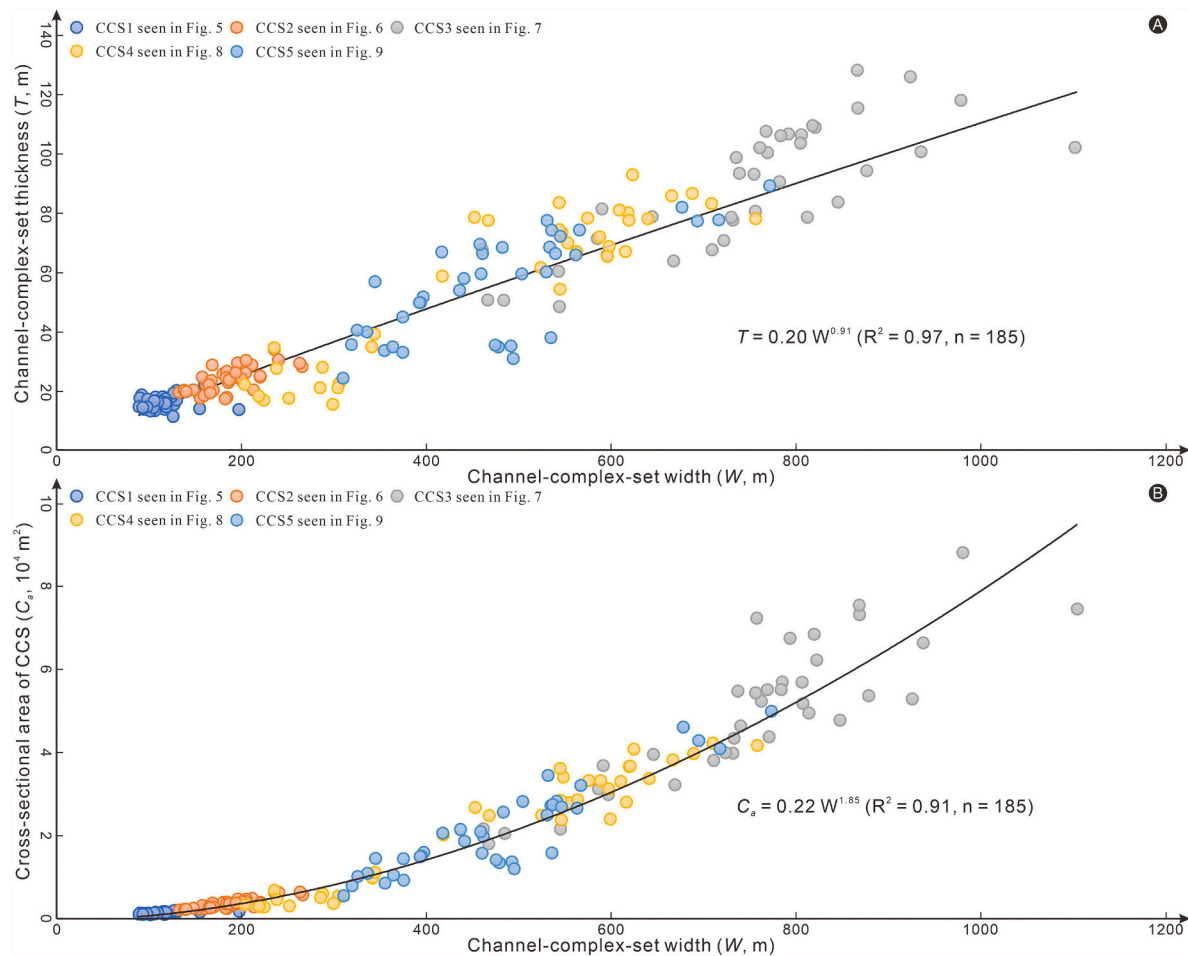


Fig. 12. Cross-plots of W versus T and W versus C_a (upper and lower panels, respectively). Note that the shown scatterplots suggest distinctive W , T , and C_a values for three discrete types of the documented CCSs. Please refer to [Tables S1–S5](#) for detailed data.

association with concomitant levees suggests a further reinterpretation of these CCSs to be aggradational leveed CCSs.

6.2. The evolution of the documented CCSs and its controls

A conceptual model consisting of three main evolutionary stages of stages 1–3 is proposed to explain the evolution of the studied channel systems in the Bay of Bengal (Fig. 15). An increase-then-decrease in channel morphometrics (represented by W , T , and C_a) from erosional non-leveed CCSs with the lowest mean values of W , T , and C_a (stage 1), to graded CCSs with the highest mean values of W , T , and C_a (stage 2), and finally, to aggradational leveed CCSs with the intermediate mean values of W , T , and C_a (stage 3) makes it reasonable to infer that the channel evolution from stages 1–3 can be related to a waxing-then-waning energy cyclicity (Fig. 15; Table 3).

Stage 1 corresponds to the waxing phase of a waxing-then-waning energy cyclicity, which is characterized by a gradual increase in flow velocity, erosive power, and flow energy (Fig. 15) (Kneller and Branney, 1995; Kneller, 2003). During this waxing energy phase, submarine channel turbidity flows became more energetic, much sandier, and increasingly more erosional (Kneller and Branney, 1995; Kneller, 2003; McHargue et al., 2011). Such properties of submarine channel turbidity

flows were recorded and evidenced by narrowest, shallowest, and areally smallest characteristics of erosional CCS1 and CCS2 expressed as purely erosional features (Figs. 9–11, and 15; Table 3). The intense erosion initiated the development and formation of straight to low-sinuosity conduits from an initially featureless slope (i.e., the condition of pre-channel substrate), giving rise to erosional non-leveed CCSs of CCS1 and CCS2 (Figs. 4, 5, 9 to 11, and 15; Table 2). Previous studies have also shown that straight, non-leveed conduits most likely created the initial conditions for channel formation (Schwenk et al., 2005; Gee et al., 2007; Sylvester et al., 2012; Maier et al., 2013; Deptuck and Sylvester, 2017).

Stage 2 corresponds to the phase of peak environmental energy in the waxing-then-waning energy cyclicity (Fig. 15). During this energy phase, submarine channel turbidity flows were most energetic, and therefore promoted the abrupt lateral offset of channel fairways (Kneller and Branney, 1995; Kneller, 1995, 2003; McHargue et al., 2011), developed graded CCSs characterized by abundant lateral migrations, crevasse splays and bend cutoffs (Figs. 6 and 9 to 11, and 15; Table 2). A transition in CCS morphometrics from erosional non-leveed CCSs (CCS1 and CCS2) with the lowest mean values of W , T , and C_a to graded CCSs (CCS3) with the highest mean values of W , T , and C_a most likely reflect an increment in flow property from waxing to waning (Fig. 15; Table 3).

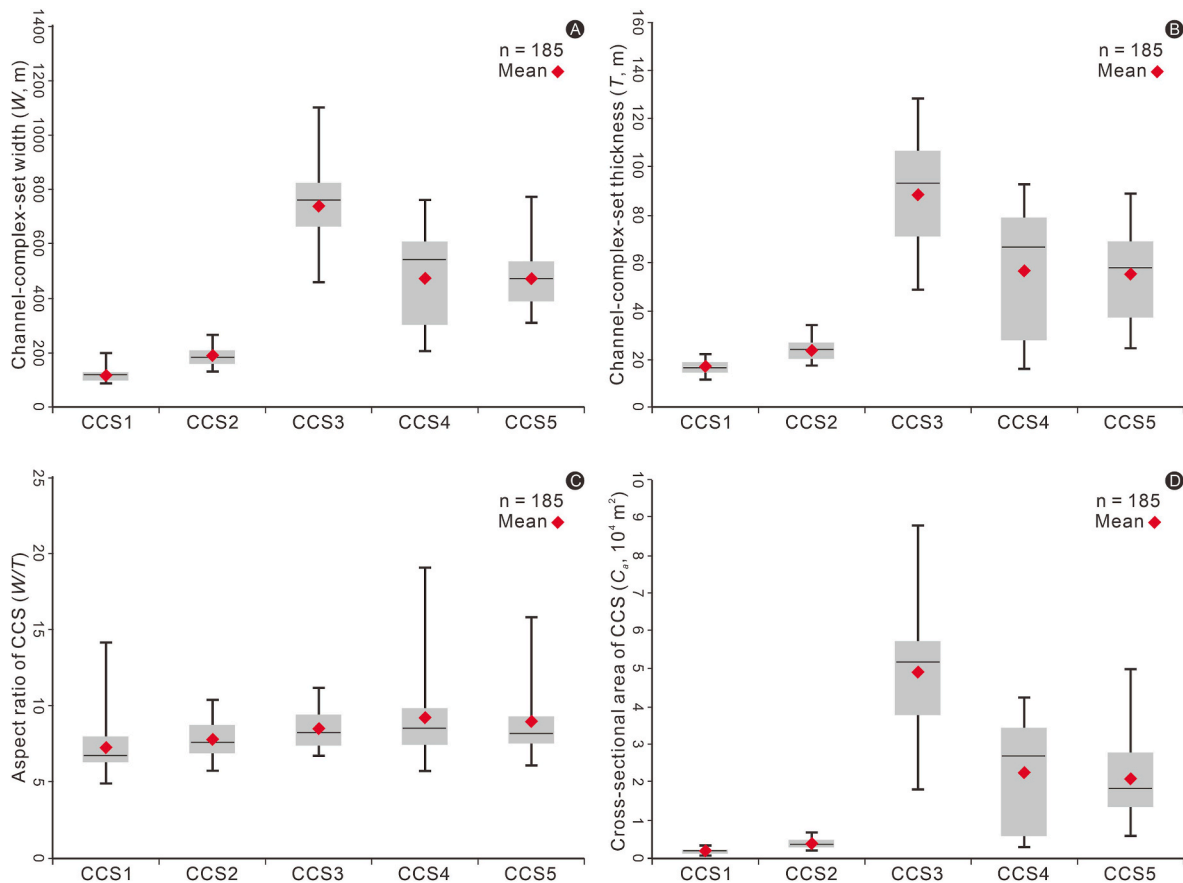


Fig. 13. Box-and-whisker plots showing the minimum, lower quartile, mean (red diamonds) median, upper quartile, and maximum asymmetry values of W (panel A), T (panel B), W/T (panel C), and C_a (panel D). Please refer to [Tables S1–S5](#) for detailed data.

CCS3 records an evolution from pre-existing non-leveed CCS1 and CCS2 to leveed CCSs (Figs. 9–11, and 15; Table 2), which are also interpreted to have evolved from non-leveed, erosional conduits by [Gee et al. \(2007\)](#), [McHargue et al. \(2011\)](#), and by [Janocko et al. \(2013\)](#).

Stage 3 corresponds to waning phase of a waxing-then-waning energy cyclicity, which is characterized by a gradual decrease in flow velocity, erosive power, and flow energy (Fig. 15) ([Kneller, 1995](#); [Kneller and Branney, 1995](#)). During this waning energy phase, submarine channel turbidity flows became more diluted, muddier, and increasingly more depositional. Such submarine channel turbidity flows encourage rapid channel-floor aggradation ([Kneller and Branney, 1995](#); [Kneller, 1995, 2003](#); [McHargue et al., 2011](#)), giving rise to aggradational leveed CCS4 and CCS5 characterized by abundant channel-floor aggradation and the widespread occurrence of crevasse splays and bend cutoffs (Figs. 7–11, and 15; Table 3; Table 2). A transition in CCS morphometrics from graded CCSs (CCS3) with the highest mean values of W , T , and C_a to aggradational leveed CCSs (CCS4 and CCS5) with the intermediate mean values of W , T , and C_a reflect a decrement in flow property from waxing to waning (Fig. 15; Table 3). Due to high rate of channel aggradation, overspill and flow stripping were dominant, resulting in volumetrically significant levees occurring along both flanks of CCS4 and CCS5 (Figs. 9–11, and 15; Table 2). Such upward increment in overbank levees (i.e., the amount of aggradation) occurs synchronously with the upward increment in CCS sinuosity (S) from stages 1–3, suggesting that channel evolution is not necessarily driven by flow

magnitude (e.g., [Sylvester et al., 2011](#)), but that channel evolution may be driven by meander development decreasing the local gradient and promoting deposition.

The above-mentioned waxing-then-waning energy cyclicity most likely triggered first incision (stage 1), then extensive lateral migration (stage 2), and finally abundant vertical aggradation (stage 3) of the studied channel systems (Fig. 15; Table 2). Such incision-to-aggradation pattern of a submarine channel evolution was recorded by incising-to-aggrading trajectory of a channel system (*sensu* [Covault et al., 2016](#)). Similar patterns of submarine channel evolution were also interpreted by [McHargue et al. \(2011\)](#), [Figueiredo et al. \(2013\)](#), and [Hodgson et al. \(2016\)](#) as the product of cycles of waxing-to-waning flow energy cyclicity.

7. Conclusions

3D seismic data from the world's largest submarine fan in the Bengal Fan are utilized to address morphological and architectural properties and evolution of a channel-levee system on the northeastern fringe of the upper Bengal Fan.

Four main types of architectural elements of the documented channel systems are recognized: (1) feeder and distributary CCSs, (2) bend cutoffs, (3) overbank levees, and (4) incised and unincised crevasse splays.

Three types of CCSs are recognized: (1) erosional non-leveed CCS1

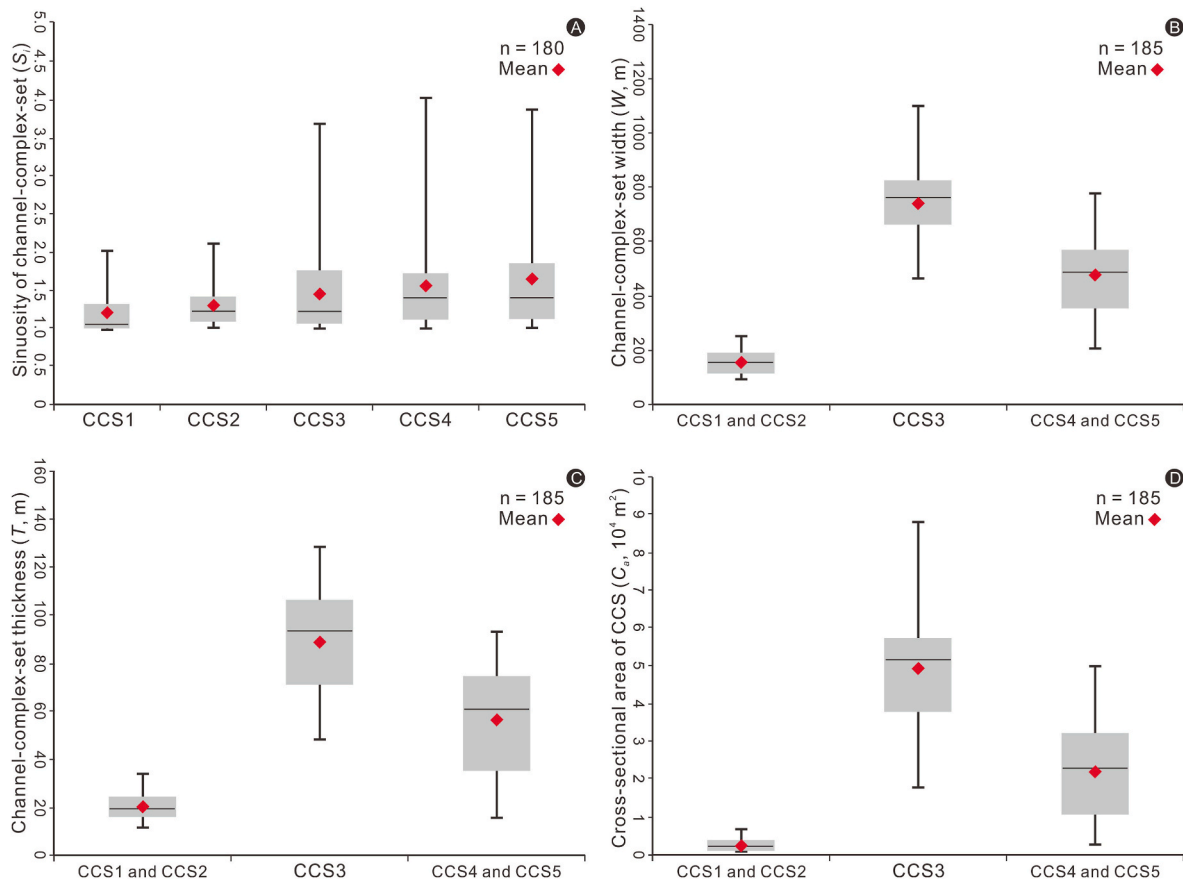


Fig. 14. Box-and-whisker plots showing the minimum, lower quartile, mean (red diamonds) median, upper quartile, and maximum asymmetry values of S_i (panel A), W (panel B), T (panel C), and C_a (panel D). Please refer to [Tables S1–S5](#) for detailed data.

Table 2

A comparison in architecture and evolution among different types of channel-complex sets, based on RGB spectral decomposition-attribute and RMS amplitude maps extracted from a horizon stack with 100 surfaces.

Type	Example	Cross-sectional geometry	Planform morphology	Associated element	Evolution event	Growth pattern
Erosional non-leveed CCSs	CCS1	Small V-shaped scours, without levees	Straight to slightly sinuous	Isolated channel fills	2 avulsion nodes, no overspill and flow stripping	Erosion
	CCS2	Small U- to V-shaped scours, without levees	Moderately sinuous	Isolated channel fills	6 avulsion nodes, no overspill and flow stripping	Amalgamation, with prominent avulsions and abrupt lateral offset of channel fairways
Graded CCSs	CCS3	Gull-wing channel form, with smaller levees	Highly sinuous	Crevasse splays and bend cutoffs	3 avulsion nodes, overspill and flow stripping	Lateral migration, with abrupt lateral offset of channel fairways
Aggradational leveed CCSs	CCS4 and CCS5	Gull-wing channel form, with larger levees	Highly sinuous, with the increased sinuosity	Crevasse splays and bend cutoffs	4 avulsion nodes, prominent overspill and flow stripping	High aggradation, with slight lateral offset of channel fairways

Table 3

A comparison in S_i , W , T , and C_a among different types of channel-complex sets, based on a set of 185 data points. Please refer to [Tables S1–S5](#) for detailed data.

Type	Example	CCS width (W , m)			CCS thickness (T , m)			CCS cross-sectional area (C_a , m ²)		
		Range	Mean	Median	Range	Mean	Median	Range	Mean	Median
Erosional non-leveed CCSs	CCS1 and CCS2	89–266	153	155	12–34	20	19	1013–6479	2613	2319
Graded CCSs	CCS3	Low			Low			Low		
		461–1102	745	761	49–128	89	93	18057–88027	49183	51792
Aggradational leveed CCSs	CCS4 and CCS5	High			High			High		
		203–772	476	487	16–93	56	61	2882–49901	21968	22635
		Intermediate			Intermediate			Intermediate		

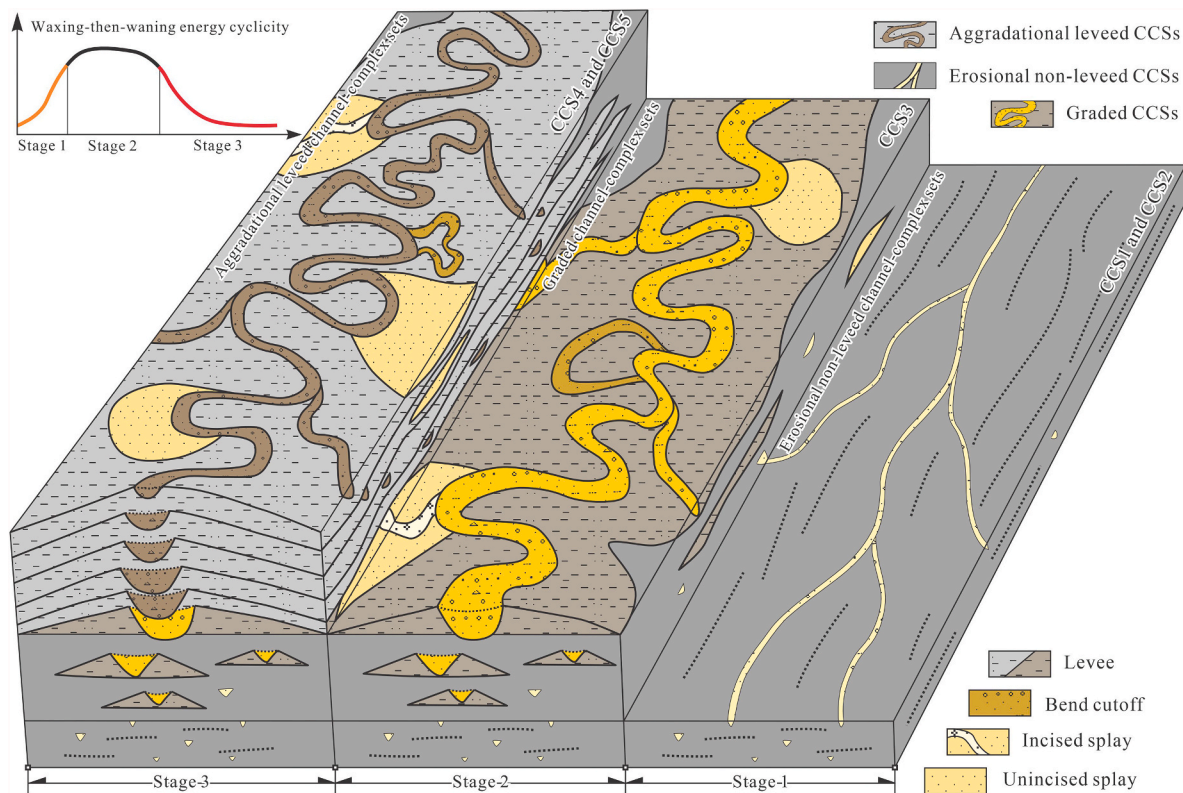


Fig. 15. Schematic illustration of the evolution of the studied channel systems and its relation to a waxing-then-waning energy cyclicality.

and CCS2 characterized by lowest mean values of $W = 153$ m, $T = 20$ m, and $C_a = 2613$ m² and by a lack of concomitant levees; (2) graded CCS3 characterized by the highest mean values of $W = 745$ m, $T = 89$ m, and $C_a = 49183$ m² and by abundant lateral migration; and (3) aggradational leveed CCS4 and CCS5 characterized by medium mean values of $W = 476$ m, $T = 56$ m, and $C_a = 21968$ m² and by abundant vertical aggradation of leveed, sinuous CCSs.

A channel evolution pattern of first incision, then extensive lateral aggradation, and followed by the abundant vertical aggradation was related to the waxing-to-waning flow energy cyclicality, as evidenced by an increase-then-decrease in channel morphometrics (represented by W , T , and C_a) from erosional non-leveed CCSs, to graded CCSs, and finally, to aggradational leveed CCSs.

During the first waxing energy phase, turbidity flows were more energetic, and increasingly more erosional, resulting in intense erosion and producing erosional non-leveed CCSs characterized by the lowest mean values of W , T , and C_a . During the second phase of peak environmental energy, turbidity currents were most energetic, giving rise to abrupt lateral offset of CCSs and resultant graded CCSs characterized by the highest mean values of W , T , and C_a . During the waning energy phase, turbidity flows were more diluted and increasingly more depositional, resulting in rapid channel-floor aggradation and resultant aggradational leveed CCSs characterized by the intermediate values of W , T , and C_a .

Declaration of competing interest

The authors declare that they have no known competing financial interests or personal relationships that could have appeared to influence the work reported in this paper.

Data availability

The data that has been used is confidential.

Acknowledgments

This research was funded by the PetroChina Hangzhou Research Institute of Geology (No. 2019D-4309). The authors thank JMPG editor (Dr. Luca Colombero), JMPG reviewers (Drs. Daniel Tek, Mike Mayall, and Daniel Bell), and an anonymous reviewer for their insightful and constructive comments, all of which significantly improved the overall quality of this study. Discussion and support of RioMar companies and University of Texas at Austin is also acknowledged. We acknowledge Chinnery Assets limited Company and Woodside for supporting our research and for giving the permission to publish this research.

Appendix A. Supplementary data

Supplementary data to this article can be found online at <https://doi.org/10.1016/j.marpetgeo.2023.106368>.

References

- Abreu, V., Sullivan, M., Pirmez, C., Mohrig, D., 2003. Lateral accretion packages (LAPs): an important reservoir element in deep water sinuous channels. *Mar. Petrol. Geol.* 20, 631–648.
- Azpiroz-Zabala, M., Cartigny, M.J., Talling, P.J., Parsons, D.R., Sumner, E.J., Clare, M.A., Simmons, S.M., Cooper, C., Pope, E.L., 2017. Newly recognized turbidity current structure can explain prolonged flushing of submarine canyons. *Sci. Adv.* 3, e1700200.
- Babonneau, N., Savoye, B., Cremer, M., Bez, M., 2004. Multiple terraces within the deep incised Zaire Valley (ZaiAngo project): are they confined levees?. In: Lomas, S.A., Joseph, P. (Eds.), *Confined Turbidite Systems*, vol. 222. Geological Society, London, Special Publications, pp. 91–114.
- Bergmann, F., Schwenk, T., Spiess, V., France-Lanord, C., 2020. Middle to late Pleistocene architecture and stratigraphy of the lower bengal fan—integrating multichannel seismic data and IODP expedition 354 results. *G-cubed* 21, e2019GC008702.
- Bouchakour, M., Zhao, X., Ge, J., Miclăuş, C., Yang, B., 2022. Evolution of submarine channel morphology in intra-slope mini-basins: 3D-seismic interpretation from offshore Niger delta. *Mar. Petrol. Geol.* 146, 105912.

- Bouchakour, M., Zhao, X., Miclăuş, C., Yang, B., 2023. Lateral migration and channel bend morphology around growing folds (Niger Delta continental slope). *Basin Res.* <https://doi.org/10.1111/bre.12750>.
- Blum, M., Rogers, K., Gleason, J., Najman, Y., Cruz, J., Fox, L., 2018. Allogenic and autogenic signals in the stratigraphic record of the deep-sea Bengal fan. *Sci. Rep.* 8, 7973.
- Bridge, J.S., 2003. *Rivers and Floodplains: Forms, Processes and Sedimentary Record*. Blackwell Publishing, Oxford, p. 491.
- Buchanan, J.Y., 1887. On the land slopes separating continents and ocean basins, especially those on the west coast of Africa. *Scott. Geogr. Mag.* 3, 217–238.
- Carter, L., Burnett, D., Drew, S., Hadorn, L., Marle, G., Bartlett-Mcneil, D., Irvine, N., 2009. Submarine cables and the oceans: connecting the world: united nations environment program, world conservation monitoring centre. *Biodiversity Series* 31, 64.
- Covault, J.A., Sylvester, Z., Hubbard, S.M., Jobe, Z.R., Sech, R.P., 2016. The stratigraphic record of submarine-channel evolution. *Sediment. Rec.* 14, 4–11.
- Clark, I.R., Cartwright, J.A., 2011. Key controls on submarine channel development in structurally active settings. *Mar. Petrol. Geol.* 28, 1333–1349.
- Clift, P., Gaedicke, C., 2002. Accelerated mass flux to the Arabian Sea during the middle to late Miocene. *Geology* 30, 207–210.
- Curry, J.R., Emmel, F.J., Moore, D.G., 2003. The Bengal Fan: morphology, geometry, stratigraphy, history and processes. *Mar. Petrol. Geol.* 19, 1191–1223.
- Daly, R.A., 1936. Origin of submarine canyons. *Am. J. Sci.* 31, 401–420.
- Deptuck, M.E., Steffens, G.S., Barton, M., Pirmez, C., 2003. Architecture and evolution of upper fan channel-belts on the Niger Delta slope and in the Arabian Sea. *Mar. Petrol. Geol.* 20, 649–676.
- Deptuck, M.E., Sylvester, Z., Pirmez, C., O'Byrne, C., 2007. Migration-aggradation history and 3-D seismic geomorphology of submarine channels in the Pleistocene Benin-major Canyon, western Niger Delta slope. *Mar. Petrol. Geol.* 23, 406–433.
- Deptuck, M.E., Sylvester, Z., 2017. Submarine fans and their channels, levees, and lobes. In: Micallef, A., Krastel, S., Savini, A. (Eds.), *Submarine Geomorphology*, pp. 273–299.
- Doughty-Jones, G., Mayall, M., Lonergan, L., 2017. Stratigraphy, facies, and evolution of deep-water lobe complexes within a salt-controlled intraslope minibasin. *AAPG (Am. Assoc. Pet. Geol.) Bull.* 101, 1879–1904.
- Edwards, C., McQuaid, S., Easton, S., Scott, D., Couch, A., Evans, R., Hart, S., 2017. Lateral accretion in a straight slope channel system: an example from the forties sandstone of the huntington field, UK central north sea. In: Bowman, M., Levell, B. (Eds.), *Petroleum Geology of NW Europe: 50 Years of Learning—Proceedings of the 8th Petroleum Geology Conference: Geological Society of London Petroleum Geology Conference Series* 8, pp. 413–428.
- Figueiredo, J.J.P., Hodgson, D.M., Flint, S.S., Kavanagh, J.P., 2013. Architecture of a channel complex formed and filled during long-term degradation and entrenchment on the upper submarine slope. In: Unit, F., Fort Brown, Fm, Karoo Basin, S.W. (Eds.), *S. Afr. Mar. Petrol. Geol.* 41, 104–116.
- Fildani, A., 2017. Submarine Canyons: A brief review looking forward: *Geology* 45, 383–384.
- Galy, V., France-Lanord, C., Beyssac, O., Faure, P., Kudrass, H., Palhol, F., 2007. Efficient organic carbon burial in the Bengal fan sustained by the Himalayan erosional system. *Nature* 450, 407–410.
- Gee, M.J.R., Gawthorpe, R.L., Bakke, K., Friedman, S.J., 2007. Seismic geomorphology and evolution of submarine channels from the Angolan continental margin. *J. Sediment. Res.* 77, 433–446.
- Gong, C., Steel, R.J., Qi, K., Wang, Y., 2021. Deep-water channel morphologies, architectures, and population densities in relation to stacking trajectories and climate states. *GSA Bulletin* 133, 287–306.
- Gong, C., Wang, H., Shao, D.L., Wang, H., Qi, K., Xu, X., 2022. How did the world's largest submarine fan in the Bay of Bengal grow and evolve at the subfan scale? *AAPG (Am. Assoc. Pet. Geol.) Bull.* 106, 1431–1451.
- Guistennec-Faugas, L., Gillet, H., Peakall, J., Dennielou, B., Gaillot, A., Jacinto, R.S., 2021. Initiation and evolution of knickpoints and their role in cut-and-fill processes in active submarine channels. *Geology* 49, 314–319.
- Hansen, L.A.S., Callow, R.H.T., Kane, I.A., Gamberi, F., Rovere, M., Cronin, B.T., Kneller, B.C., 2015. Genesis and character of thin-bedded turbidites associated with submarine channels. *Mar. Petrol. Geol.* 67, 852–879.
- Hansen, L., Janocko, M., Kane, I., Kneller, B., 2017. Submarine channel evolution, terrace development, and preservation of intra-channel thin-bedded turbidites: mahin and Avon channels, offshore Nigeria. *Mar. Geol.* 383, 146–167.
- Heijnen, M.S., Clare, M.A., Cartigny, M.J.B., Talling, P.J., Hage, S., Lintern, D.G., Stacey, C., Parsons, D.R., Simmons, S.M., Chen, Y., Sumner, E.J., Dix, J.K., Hughes Clarke, J.E., 2020. Rapidly-migrating and internally-generated knickpoints can control submarine channel evolution. *Nat. Commun.* 11, 3129.
- Hodgson, D.M., Kane, I.A., Flint, S.S., Brunt, R.L., Ortiz-Karpf, A., 2016. Time-transgressive confinement on the slope and the progradation of basin-floor fans: implications for the sequence stratigraphy of deep-water deposits. *J. Sediment. Res.* 86, 73–86.
- Hage, S., Galy, V.V., Cartigny, M.J.B., Acikalin, S., Clare, M.A., Gröcke, D.R., Hilton, R. G., Hunt, J.E., Lintern, D.G., McGhee, C.A., Parsons, D.R., Stacey, C.D., Sumner, E.J., Talling, P.J., 2020. Efficient preservation of young terrestrial organic carbon in sandy turbidity-current deposits. *Geology* 48, 882–887.
- Howlett, D.M., Gawthorpe, R.L., Ge, Z., Rotevatn, A., Jackson, C.A.-L., 2021. Turbidites, topography and tectonics: evolution of submarine channel-lobe systems in the salt-influenced Kwanza Basin, offshore Angola. *Basin Res.* 33, 1076–1110.
- Hubbard, S.M., Romans, B.W., Fildani, A., 2011. The stratigraphic evolution of deep-water architecture (thematic volume editorial). *Mar. Petrol. Geol.* 28, 609–611.
- Hughes Clarke, J.E., 2016. First wide-angle view of channelized turbidity currents links migrating cyclic steps to flow characteristics. *Nat. Commun.* 7, 11896.
- Janocko, M., Nemec, W., Henriksen, S., Warchol, M., 2013. The diversity of deep-water sinuous channel belts and slope valley-fill complexes. *Mar. Petrol. Geol.* 41, 7–34.
- Jobe, Z.R., Sylvester, Z., Parker, A.O., Howes, N., Slowey, N., Pirmez, C., 2015. Rapid adjustment of submarine channel architecture to changes in sediment supply. *J. Sediment. Res.* 85, 729–753.
- Kane, I., Kneller, B., Dykstra, M., Kassem, A., McCaffrey, W.D., 2007. Anatomy of a submarine channel-levee: an example from Upper Cretaceous slope sediments. Rosario Formation, Baja California, Mexico: *Mar. Petrol. Geol.* 24, 540–563.
- Kneller, B.C., 1995. Beyond the turbidite paradigm: physical models for deposition of turbidites and their implications for reservoir prediction. In: Hartley, A.J., Prosser, D.J. (Eds.), *Characterization of Deep Marine Clastic Systems*. Geological Society of London Special Publication, pp. 31–49.
- Kneller, B.C., Branney, M.J., 1995. Sustained high-density turbidity currents and the deposition of thick massive sands. *Sedimentology* 42, 607–616.
- Kneller, B., 2003. The influence of flow parameters on turbidite slope channel architecture. *Mar. Petrol. Geol.* 20, 901–910.
- Kolla, V., Bourges, P., Urruty, J.-M., Safa, P., 2001. Evolution of deepwater sinuous channels offshore Angola (west Africa) and implications for reservoir architecture. *AAPG (Am. Assoc. Pet. Geol.) Bull.* 85, 1373–1405.
- Kolla, V., 2007. A review of sinuous channel avulsion patterns in some major deep-sea fans and factors controlling them. *Mar. Petrol. Geol.* 24, 450–469.
- Lowe, D.R., Graham, S.A., Malkowski, M.A., Das, B., 2019. The role of avulsion and splay development in deep-water channel systems: sedimentology, architecture, and evolution of the deep-water Pliocene Godavari “A” channel complex. *Mar. Petrol. Geol.* 105, 81–99. India.
- Ma, H.X., Fan, G.Z., Shao, D.L., Ding, L.B., Sun, H., Zhang, Y., Zhang, Y.G., Cronin, B.T., 2020. Deep-water depositional architecture and sedimentary evolution in the Rakhine Basin, northeast Bay of Bengal. *Petrol. Sci.* 17, 598–614.
- Maier, K.L., Fildani, A., Paull, C.K., McHargue, T.R., Graham, S.A., Caress, D.W., 2013. Deep-sea channel evolution and stratigraphic architecture from inception to abandonment from high-resolution Autonomous Underwater Vehicle surveys offshore central California. *Sedimentology* 60, 935–960.
- Mattern, F., 2005. Ancient sand-rich submarine fans: depositional systems, models, identification, and analysis. *Earth Sci. Rev.* 70, 167–202.
- Mayall, M., Jones, E., Casey, M., 2006. Turbidite channel reservoirs—Key elements in facies prediction and effective development. *Mar. Petrol. Geol.* 23, 821–841.
- Mayall, M., Lonergan, L., Bowman, A., 2010. The response of turbidite slope channels to growth-induced seabed topography. *AAPG (Am. Assoc. Pet. Geol.) Bull.* 94, 1011–1030.
- McHargue, T., Pyrcz, M.J., Sullivan, M.D., Clark, J.D., Fildani, A., Romans, B.W., Covault, J.A., Levy, M., Posamentier, H.W., Drinkwater, N.J., 2011. Architecture of turbidite channel-levee systems on the continental slope: patterns and predictions. *Mar. Petrol. Geol.* 28, 728–743.
- Mitchell, W.H., Whittaker, A.C., Mayall, M., Lonergan, L., 2021a. New models for submarine channel deposits on structurally complex slopes: examples from the Niger delta system. *Mar. Petrol. Geol.* 129, 1–22.
- Mitchell, W.H., Whittaker, A.C., Mayall, M., Lonergan, L., Pizzi, M., 2021b. Quantifying the relationship between structural deformation and the morphology of submarine channels on the Niger Delta continental slope. *Basin Res.* 33, 186–209.
- Oluboyo, A.P., Gawthorpe, R.L., Bakke, K., Hadler-Jacobsen, F., 2014. Salt tectonic controls on deep-water turbidite depositional systems: miocene, southwestern lower Congo basin, offshore Angola. *Basin Res.* 26, 597–620.
- Othman, A.A.A., Fathy, M., Maher, A., 2016. Use of spectral decomposition technique for delineation of channels at solar gas discovery, offshore West Nile Delta, Egypt. *Egyptian Journal of Petroleum* 25, 45–51.
- Paull, C.K., Talling, P.J., Maier, K.L., Parsons, D., Xu, J., Caress, D.W., Gwiazda, R., Lundsten, E.M., Anderson, K., Barry, J.P., Chaffey, M., O'Reilly, T., Rosenberger, K. J., Gales, J.A., Kieft, B., McGann, M., Simmons, S.M., McCann, M., Sumner, E.J., Clare, M.A., Cartigny, M.J., 2018. Powerful turbidity currents driven by dense basal layers. *Nat. Commun.* 9, 4114.
- Paumard, V., Bourget, J., Duro, B., Lacaze, S., Payenberg, T., George, A.D., Lang, S., 2019. Full-volume 3D seismic interpretation methods: a new step towards high-resolution seismic stratigraphy. *Interpretation* 7, B33–B47.
- Paumard, V., Bourget, J., Payenberg, T., George, A., Ainsworth, R.B., Lang, S., Posamentier, H., 2020. Controls on deep-water sand delivery beyond the shelf edge: accommodation, sediment supply, and deltaic process regime. *J. Sediment. Res.* 90, 104–130, 2020.
- Peakall, J., Sumner, E.J., 2015. Submarine channel flow processes and deposits: a process-product perspective. *Geomorphology* 244, 95–120.
- Pickering, K.T., Carter, A., Andò, S., Garzanti, E., Limonta, M., Vezzolici, G., Milliken, K. L., 2020. Deciphering relationships between the Nicobar and Bengal submarine fans. *Indian Ocean: Earth Planet Sci. Lett.* 544, 116329.
- Posamentier, H.W., Kolla, V., 2003. Seismic geomorphology and stratigraphy of depositional elements in deep-water settings. *J. Sediment. Res.* 73, 367–388.
- Posamentier, H.W., Paumard, V., Lang, S.C., 2022. Principles of seismic stratigraphy and seismic geomorphology I: extracting geologic insights from seismic data. *Earth Sci. Rev.* 228, 103963.
- Prins, M.A., Postma, G., 2000. Effects of climate, sea level, and tectonics unraveled for last deglaciation turbidite records of the Arabian Sea. *Geology* 28, 375–378.
- Qin, Y., Alves, T.M., Constantine, J.A., Gamboa, D., Wu, S., 2020. Effect of channel tributaries on the evolution of submarine channel confluences (Espírito Santo Basin, SE Brazil). *GSA Bulletin* 132, 263–272.

- Schwenk, T., Spieß, V., Breitzke, C., Hübscher, C., 2005. The architecture and evolution of the Middle Bengal Fan in vicinity of the active channelevee system imaged by high-resolution seismic data. *Mar. Petrol. Geol.* 22, 637–656.
- Shepard, F.P., Emery, K.O., 1941. Submarine Topography off the California Coast: Canyons and Tectonic Interpretations. Geological Society of America Special Paper, p. 171.
- Sylvester, Z., Pirmez, C., Cantelli, A., 2011. A model of submarine channel-levee evolution based on channel-growth trajectories: implications for stratigraphic architecture. *Mar. Petrol. Geol.* 28, 716–717.
- Sylvester, Z., Deptuck, M.E., Prather, B., Prather, B.E., Pirmez, C., O'byrne, C., 2012. Seismic stratigraphy of a shelf-edge delta and linked submarine channels in the NE Gulf of Mexico. In: Prather, B., Deptuck, M., Mohrig, B., Hoorn, B.V., Wynn, R.B. (Eds.), *Application of the Principles of Seismic Geomorphology to Continental Slope and Base-Of-Slope Systems: Case Studies from Seafloor and Near-Seafloor Analogues*, vol. 99. SEPM Special Publication, pp. 31–59.
- Sylvester, Z., Covault, J.A., 2016. Development of cutoff-related knickpoints during early evolution of submarine channels. *Geology* 44, 835–838.
- Symons, W.O., Sumner, E.J., Paull, C.K., Cartigny, M.J.B., Xu, J.P., Maier, K.L., Lorensen, T.D., Talling, P.J., 2017. A new model for turbidity current behavior based on integration of flow monitoring and precision coring in a submarine canyon. *Geology* 45, 367–370.
- Tek, D.E., McArthur, A.D., Poyatos-Moré, M., Colombero, L., Patacci, M., Craven, B., McCaffrey, W., 2021. Relating seafloor geomorphology to subsurface architecture: how mass-transport deposits and knickpoint-zones build the stratigraphy of the deep-water Hikurangi Channel. *Sedimentology* 68, 3141–3190.
- Vendettuoli, D., Clare, M.A., Hughes Clarke, J.E., Vellinga, A., Hizzet, J., Hage, S., Cartigny, M.J.B., Talling, P.J., Waltham, D., Hubbard, S.M., Stacey, C., Lintern, D.G., 2019. Daily bathymetric surveys document how stratigraphy is built and its extreme incompleteness in submarine channels. *Earth Planet Sci. Lett.* 515, 231–247.
- Wynn, R.B., Cronin, B.T., Peakall, J., 2007. Sinuous deep-water channels: genesis, geometry and architecture. *Mar. Petrol. Geol.* 24, 341–387.
- Yang, S.Y., Kim, J.W., 2014. Pliocene basin-floor fan sedimentation in the Bay of Bengal (offshore northwest Myanmar). *Mar. Petrol. Geol.* 49, 45–58.
- Zhou, L., Sun, Z., Tang, G., Xiao, D., Cai, Z., Wang, H., Su, J., Hua, S., Ge, W., Chen, C., 2020. Pliocene Hyperpycnal Flow and its Sedimentary Pattern in D Block of Rakhine Basin in Bay of Bengal. *Petroleum Exploration and Development*, pp. 318–330.